

**Tunable and broadband S-band loop-gap-resonator
for nitrogen vacancy centers in diamond**

by

Erik Roger Eisenach

B.S., The Citadel, The Military College of South Carolina (2015)

Submitted to the Department of Electrical Engineering and Computer
Science

in partial fulfillment of the requirements for the degree of
Master of Science in Electrical Engineering and Computer Science

at the

MASSACHUSETTS INSTITUTE OF TECHNOLOGY

June 2018

© Massachusetts Institute of Technology 2018. All rights reserved.

Author
Department of Electrical Engineering and Computer Science
May 23, 2018

Certified by
Dirk Englund
Associate Professor, Massachusetts Institute of Technology
Thesis Supervisor

Certified by
Danielle Braje
Assistant Group Leader, Lincoln Laboratory
Thesis Supervisor

Accepted by
Leslie A. Kolodziejski
Chairman, Department Committee on Graduate Theses

**Tunable and broadband S-band loop-gap-resonator for
nitrogen vacancy centers in diamond**

by

Erik Roger Eisenach

Submitted to the Department of Electrical Engineering and Computer Science
on May 23, 2018, in partial fulfillment of the
requirements for the degree of
Master of Science in Electrical Engineering and Computer Science

Abstract

In this thesis, the loop gap resonator (LGR) is presented as a mechanism for the delivery of resonantly enhanced and uniform microwave fields to large volume samples of nitrogen vacancy (NV) centers in diamond. Specifically, an S-band tunable LGR and its constituent excitation circuitry are designed that allow directionally uniform, strong, homogeneous, and broadband microwave (MW) driving of an NV ensemble over an area larger than 32 mm^2 . Two methods of coupling to the resonator are implemented and discussed. The LGR design, based on the anode block of a cavity magnetron, demonstrates an average field amplitude of 5 gauss at 42 dBm of input power, and achieves a peak-to-peak field uniformity of 89.5% over an area of 32.2 mm^2 and 97% over an area of 11 mm^2 . The broad bandwidth of the LGR is capable of addressing all resonances of an NV ensemble for bias magnetic Fields up to 20 gauss. Furthermore, with cavity ring-down-times in the single nanoseconds, the resonator is compatible with the pulsed MW techniques necessary for a wide range of NV-diamond applications.

Thesis Supervisor: Dirk Englund
Title: Associate Professor, Massachusetts Institute of Technology

Thesis Supervisor: Danielle Braje
Title: Assistant Group Leader, Lincoln Laboratory

Acknowledgments

This is the acknowledgements section. You should replace this with your own acknowledgements.

Contents

1 The Nitrogen Vacancy Center in Diamond	15
1.1 Introduction	15
1.2 The NV Physical and Electronic Structure	16
1.3 NV magnetometry	17
1.3.1 Vector Magnetometry with NV Centers	18
1.3.2 Continuous Wave Magnetometry	19
1.3.3 Pulsed Ramsey-type Magnetometry	20
1.4 Rabi oscillations	22
2 The Loop Gap Resonator	25
2.1 Resonant Enhancement of the MW field	26
2.2 Model	27
2.2.1 Equivalent circuit picture	27
2.2.2 Solution to Maxwell's equations	29
2.3 LGR Design	31
2.3.1 LGR	31
2.3.2 Tuning	35
2.3.3 Excitation Design	35
2.4 Electric Field	39
3 LGR Performance and Field Characterization	41
3.1 Quality Factor	41
3.1.1 Ringdown time	42

3.2	Simulating the Magnetic Field	43
3.3	Measuring the Magnetic Field	45
3.3.1	Experimental setup	49
3.3.2	Measurement process	51
3.4	LGR field distribution	53
4	Discussion and Outlook	55
A	LGR variations	57
A.1	Smaller Cavity LGR	57
A.2	Copper LGR	58
A.3	Shielding	59

List of Figures

1-1	The NV center a) The NV level structure b) One of four crystal orientations of the NV.	18
1-2	ESR resonances ESR resonances of a single NV orientation split by an ambient magnetic field B_z . Parameters in plot correspond to sensitivity formula in equation 1.3.	20
1-3	Pulsed Magnetometry Sequences a) Ramsey Sequence for DC magnetometry b) Hahn-Echo Sequence for AC magnetometry.	22
1-4	Rabi pulse sequence and oscillations a) Pulse sequence for detecting Rabi oscillation between two spin sublevels b) Example Rabi oscillations (—) with exponential decay envelope (---).	23
2-1	LGR dimensions Geometrical parameters of LGR used in sections 2.2.1 and 2.2.2	27
2-2	LGR equivalent circuit diagram Diagram showing equivalent inductance and capacitance of LGR and their connections.	28
2-3	Loop Gap Resonator Variations a) Hole and Slot. b) Slot. c) Vane. d) Rising Sun - type	32
2-4	Rendering and Wire Diagram of Loop Gap Resonator a) The metallic resonator employs a five-loop four-gap architecture. Microwaves are coupled into the LGR via the exciter antenna, which is fabricated on a printed circuit board. b) Line drawing of the LGR. All dimensions are in mm. Optional mounting holes and radial access port for laser excitation are now shown.	33

2-5	Eigenfrequency solution to LGR TE ₁₀ mode located at $f_0 \approx 4.6$ GHz. The outer loops are oscillating π radians out of phase with center loop.	34
2-6	3D Rendering of coupling loop and scattering parameter for different coupling configurations a) Rendering of lateral coupling loop and LGR. b) Scattering parameter S_{11} for different coupling configurations. Critically coupled (—) at $z \approx 1$ mm, under-coupled (—) at $z \approx 1.25$ mm, over-coupled (—).	36
2-7	Exciter board drawing A feedline, 50:50 power splitter, and balun (balanced unbalanced) feed the split ring resonator, which is coupled to the LGR. All dimensions are in mm. Optional mounting holes and radial access port for laser excitation are not shown	37
2-8	Frequency tuning and impedance matching of LGR composite device. (a) The resonant frequency f_0 is adjusted by translating the sapphire shims in the four capacitive gaps. In the absence of a stub tuner, the LGR composite device exhibits S_{11} values between -10 and -20 dB from 2.5 to 3.5 GHz, indicating at least $\gtrsim 90\%$ of power delivered to the LGR composite device contributes to B_1 in this range. (b) Nearly perfect critical coupling can be achieved with a stub tuner, allowing practically all incident MW power to contribute to B_1	38
2-9	Simulated electric field magnitude E in vicinity of LGR capacitive gap. Inset depicts the electric field magnitude E as a function of distance from the capacitive gap with $x' = 0$ mm corresponding to the plane of the central loop-gap interface.	39

3-1	Simulated magnetic field Top-down cross section of center loop of LGR. Slice is taken at half height h . Simulations suggest the B_1 field distribution should be approximately radially symmetric, with the leading order deviation resulting from the exciter antenna. Dashed lines indicate the 32 mm^2 and 11mm^2 areas within which the B_1 field uniformity is evaluated.	44
3-2	Simulated B_1 field along LGR symmetry axis. The symmetry plane of the LGR is located at $z = 0 \text{ mm}$. The edges of the LGR are at $z = \pm 2.5 \text{ mm}$, and the split-ring resonator is located at $z = 4.024 \text{ mm}$. The presence of the split-ring resonator shifts the point of maximal B_1 off-center to $z_0 = -0.4 \text{ mm}$	45
3-3	B_z component of field measured with probe a) 3D surface plot of B_z field distribution using a Beehive 100B magnetic field probe. Color bar units are normalized magnetic field. Normalized to their maximum value. b) Same data as in a) but top-down view.	47
3-4	Confocal Microscope Custom built confocal microscope used to measure B_1 in LGR.	48
3-5	Image of Scanning Confocal Microscope Custom built scanning confocal microscope used to measure the B_1 distribution in the LGR	50

3-6 LGR driving of an NV ensemble (a) NV electron spin resonance spectrum (—) under application of bias field B_0 . The bias field allows individual addressing of all eight NV resonances, arising from the combination of the two allowed magnetic dipole transitions with the four possible NV orientations. The NV hyperfine structure is obscured by MW power broadening and the contrast variation between the NV resonances is attributed primarily to the S_{11} line-shape. The S_{11} parameter is shown before (---) and after (---) shifting the LGR resonant frequency f_0 to the target NV resonance. Arrows indicate corresponding y axes. (b) Typical data depicting Rabi oscillations under MW excitation at the target NV resonance frequency indicated in (a). Data (o) is fit (—) to an exponentially decaying sinusoid.	52
3-7 Locus of Measurement Points An NV-containing 4.5 mm × 4.5 mm diamond plate is placed in the LGR central loop, and the Rabi frequency is measured where indicated (●,●,●,●) to characterize B_1	53
3-8 B_1 field uniformity of LGR composite device. B_1 field measurements (○,○,○,○) at the points depicted in 3-7 and simulations (—,—,—,—) along each locus of points are in good agreement. Error bars indicate 1-sigma uncertainty for the B_1 measurement. Dashed lines indicate the radial boundaries of the 32 mm ² and 11 mm ² areas over which B_1 field uniformity is evaluated. The measured B_1 uniformity is given for each area.	54
A-1 Smaller LGR design (a) Line drawing of smaller LGR with central loop radius $r_c = 2.5$ mm as described in section A.1. Units are in mm. (b) Measured S_{11} for composite device tuned to $f_0 \approx 2.87\text{GHz}$	57
A-2 Copper Loop Gap Resonator Loop Gap Resonator manufactured from C145 machinable copper	58
A-3 Copper vs. Titanium LGR Scattering parameters (S_{11}) of the copper manufactured LGR (—) in comparison to titanium LGR (—)	59

List of Tables

2.1 Some modes the LGR supports and their measured vs. simulated frequencies. Many separate modes are degenerate due to their symmetrical nature. Additionally	34
--	----

Chapter 1

The Nitrogen Vacancy Center in Diamond

1.1 Introduction

The nitrogen-vacancy (NV) defect center in diamond is currently of great interest for many applications in quantum sensing [72, 4, 22, 53, 18, 34] and quantum information [11, 28, 24] due to its many outstanding properties, which include long room temperature coherence times [4] and simplicity of optical quantum state initialization and readout [65, 39]. An active area of effort is NV magnetometry, with recent demonstrations of measurement modalities ranging from scanning magnetic microscopy [18] to wide-field imaging [58] to bulk magnetometry [77]. Many of these modalities address ensembles of NV centers and therefore require strong and uniform microwave (MW) field driving, often over mm length scales. In this thesis I discuss the design considerations of a suitable MW delivery mechanism, fabricate a hole-and-slot type loop gap resonator (LGR), and evaluate its performance for NV applications.

As an introduction to the field of quantum sensing using NV centers Chapter 1, The Nitrogen Vacancy Center in Diamond, introduces the photophysics of the NV¹; the NV's use in continuous wave and pulsed vector magnetometry; the sensitivity

¹A detailed derivation of the NV level structure using group theoretic approach can be found in [19, 20, 46]

achievable in both schemes; and Rabi oscillations between ground state sub-levels in the NV electronic structure.

Chapter 2, The Loop Gap Resonator, discusses resonant enhancement of MW field strengths in resonators; introduces an analytical model of the loop gap resonator (LGR) used to compute resonant frequency, field strength and homogeneity; outlines the design of an LGR for use in NV magnetometry; and briefly discusses the effect of dielectric samples in the center cavity on the LGR resonant frequency.

Chapter 3, LGR Performance and Field Characterization, discusses the importance of the resonator quality factor on its ring down time and, consequently, on pulsed NV magnetometry schemes, simulations of the LGR magnetic field distribution in the mode of interest, the experimental setup and process used to measure the field within the LGR, and the outcome of measurements determined to experimentally determine the field within the LGR center cavity.

Chapter 4, Discussion and Outlook, takes a look at how the LGR can be implemented as a universal MW solution for NV centers and provides a outlook on future developments such as higher Q resonators and planar LGR structures for improved optical access.

1.2 The NV Physical and Electronic Structure

The NV color center is a deep band gap impurity within the diamond crystal lattice. It consists of a nitrogen atom and a vacancy sitting in adjacent diamond lattice sites [Figure 1-1 (b)]. In low strain diamond, there exist four possible orientations that are equally likely to be populated. The NV can occur primarily in two charge states NV^{-1} and NV^0 of which only the first is useful for many applications such as quantum sensing and quantum computing. The NV^{-1} (simply denoted as NV from here on out) happens to benefit from favorable optical and spin properties which are explained in detail in the sections below. The NV's inclusion in the C_{3v} point group permits a 3A_2 symmetric spin-triplet ground electronic state and an excited 3E state separated by a zero phonon line (ZPL) of 637nm [Fig 1-1 (a)] [46]. The ground state spin triplet

is split via spin-spin interactions giving rise to a zero field splitting separating the $|m_s = 0\rangle$ from the $|m_s = \pm 1\rangle$ states by 2.87GHz (D_{gs}). The ground electronic structure is modeled effectively by following Hamiltonian (neglecting hyperfine interactions with nearby nuclear spins),

$$\mathcal{H}_{gs} = \hbar D_{gs} S_z^2 + \hbar E_{gs} (S_x^2 + S_y^2) + \underbrace{g_s \mu_B \mathbf{B} \cdot \mathbf{S}}_{\mathcal{H}_{Zeeman}}, \quad (1.1)$$

Where we define z to be the NV quantization axis, \hbar is the Planck constant, D_{gs} and E_{gs} are the ground state axial and transverse splitting parameters (respectively), S_x , S_y , and S_z the Pauli spin matrices, g_s the electron Landé g-factor, μ_B the Bohr magneton, and \mathbf{B} an externally applied magnetic field. Solving for the eigenenergies of the Hamiltonian yields the electron spin resonance (ESR) frequencies [Figure 1-2]. \mathcal{H}_{Zeeman} can be split further into parallel and perpendicular components,

$$\mathcal{H}_{Zeeman} = \mathcal{H}_{\parallel} + \mathcal{H}_{\perp} = \underbrace{g_s \mu_B B_z}_{\mathcal{H}_{\parallel}} + \underbrace{g_s \mu_B (B_x S_x + B_y S_y)}_{\mathcal{H}_{\perp}}. \quad (1.2)$$

of which, in the weak magnetic field regime, \mathcal{H}_{\parallel} is the dominating term. In this regime the ESR frequencies evolve quadratically with an applied field if $g_s \mu_B B_z \sim \hbar E_{gs}$ and linearly if $g_s \mu_B B_z \gg \hbar E_{gs}$ [62]. Therefore, to practice magnetometry (explained in more detail in the following sections), it's most useful to apply a biasing field in order to reach a linear dependence of the ESR frequencies on the magnetic field.

1.3 NV magnetometry

Application of a static biasing magnetic field B_0 splits the $|m_s = \pm 1\rangle$ levels via Zeeman interaction (equation 1.1) proportional to the projection of the field onto the NV symmetry axis. When the NV is driven into one of these states and optically excited (generally achieved using 532nm CW or pulsed laser) it undergoes phononic-relaxation and settles into the corresponding sublevel of the excited state. These sublevels allow the NV to preferentially decay back down to the $|0\rangle$ ground state via an inter-system

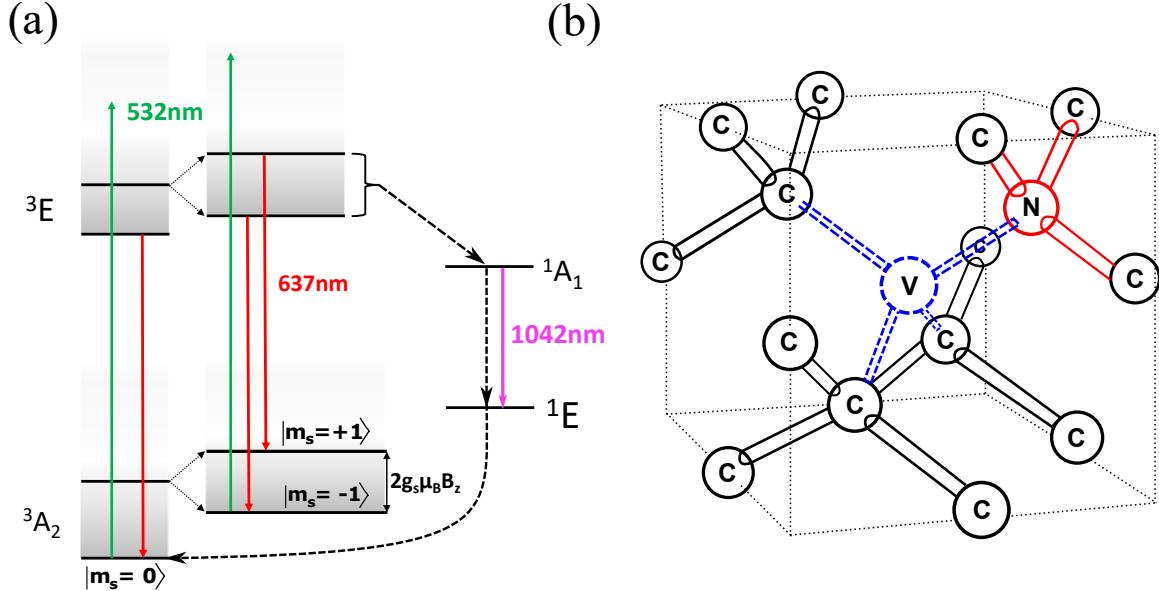


Figure 1-1: **The NV center** **a)** The NV level structure **b)** One of four crystal orientations of the NV.

crossing and metastable state which are separated in the infrared [Figure 1-1]. This non-spin-conserving process therefore provides the mechanism of spin polarizing the NV for continued MW driving. The simplest method of reading out the NV spin state is by sweeping the driving microwave field and monitoring NV fluorescence in the visible band. A drop in fluorescence at a particular driving frequency indicates electron spin resonance (ESR) which can be monitored via lock-in amplification for any detuning due to a change in the external field [39, 62]. Since the NV can exist in one of four possible orientations—each orientation being equally likely—the ESR can be separated into eight distinct non-degenerate resonances which probe different field components. The various orientations act as basis vectors which collectively span the space and allow the total vector field to be reconstructed [39].

1.3.1 Vector Magnetometry with NV Centers

As mentioned in section 1.2, the C_{3v} symmetry of diamond allows NV centers to be aligned in four different orientations in the lattice. Since, at fields lower than 10 mT, the Zeeman splitting of the $|\pm 1\rangle$ is proportional to the vector field projection along

the NV symmetry axis² (B_z) the energy shifts can be determined by $g_s\mu_B \mathbf{B} \cdot \mathbf{u}_n$, where \mathbf{u}_n ($n = 1, 2, 3, 4$) is the unit vector along the n^{th} NV axis. By either sequentially [14] or simultaneously [66, 42] measuring the Zeeman splitting between either the $|0\rangle \leftrightarrow |+1\rangle$ or $|0\rangle \leftrightarrow |-1\rangle$ ³ transitions of all four orientations, one can reconstruct the total vector field by generating the vector components (B_x , B_y , and B_z) from the projection along each of the crystallographic axes [42, 66].

1.3.2 Continuous Wave Magnetometry

For continuous wave magnetometry the ESR frequencies are continuously monitored (often using lock in amplification) since the external magnetic field is imprinted in their spectral positions ω_+ and ω_- [Fig 1-2]. As mentioned in section 1.3.1, the four orientations of the NV in the diamond crystal lattice therefore result in eight distinct resonances when split by an external biasing field (B_0). Monitoring a minimum of three out of four resonances allows for the full vector reconstruction of the field. An infinitesimal additional magnetic field variation δB shifts the resonances away from the known spectrum and the change in NV fluorescence, which is given by $(\frac{\partial \beta}{\partial B}) \cdot \delta B \cdot \tau$ [62], is measured in the laboratory. The shot-noise limited sensitivity is then given as,

$$\eta_{cw} \approx \mathcal{P}_{\mathcal{F}} \frac{\hbar}{g_s \mu_B} \frac{\Delta\omega \sqrt{\tau}}{C \sqrt{N\beta}}. \quad (1.3)$$

Where $\mathcal{P}_{\mathcal{F}}$ is a numerical factor determined by the NV ESR lineshape⁴, C is the measurement contrast, $\Delta\omega$ is the linewidth, τ the integration time, β the fluorescence collected per NV per measurement, and N the number of NVs addressed. The signal contrast C can be increased by driving the NV with stronger MW fields at the expense of power-broadening the linewidth $\Delta\omega$. However, the linewidth can be decreased down

²At these low fields the terms in the NV Hamiltonian (see equation 1.1) that are proportional to the perpendicular component of the field are suppressed to order $\sim B_{xy}^2/D_{gs}$ and can therefore be neglected[72]

³The transition $|-1\rangle \leftrightarrow |+1\rangle$ can also be employed which yields the benefit that the energy shift becomes $2g_s\mu_b\mathbf{B}$ and therefore provides twice the signal over the other two transitions while simultaneously mitigating temperature effects [53]. However, this requires treatment of the full three-level spin system since the $|-1\rangle \leftrightarrow |+1\rangle$ splitting is a non-dipole allowed transition.

⁴ $\mathcal{P}_{\mathcal{F}} = 4/3\sqrt{3}$ for a Lorentzian lineshape and $\mathcal{P}_{\mathcal{F}} = \sqrt{e/8\ln 2}$ for a gaussian lineshape (see [57])

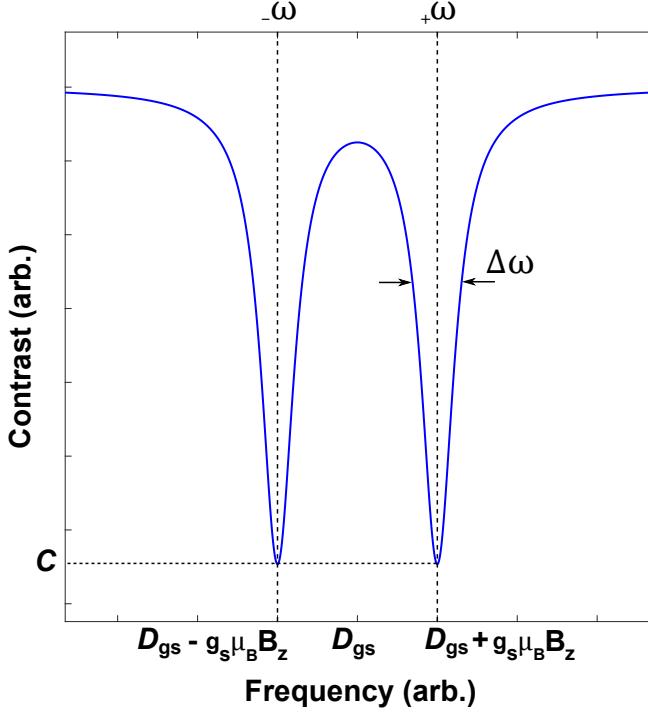


Figure 1-2: **ESR resonances** ESR resonances of a single NV orientation split by an ambient magnetic field B_z . Parameters in plot correspond to sensitivity formula in equation 1.3.

to a limit given the inhomogeneous dephasing time T_2^* by reducing the laser and MW excitation strength [23], effectively decreasing the number of collected photons per measurement β . An optimization of contrast C , linewidth $\Delta\omega$, and collection β yields an optimized sensitivity of [57]

$$\eta_{cw} \approx \mathcal{P}_{\mathcal{F}} \frac{2\hbar}{g_s \mu_B} \frac{1}{C \sqrt{N \beta T_2^*}}. \quad (1.4)$$

1.3.3 Pulsed Ramsey-type Magnetometry

Strong microwave driving in a CW experiment broadens the ESR linewidth causing a reduction in magnetometer sensitivity. To take advantage of strong driving fields without incurring the effects of MW or pump laser power broadening, DC fields can be measured using a Ramsey pulse sequence. In this scheme microwave driving, spin polarization and sensing are all separated in time [Fig 1-3(a)]. After spin polarizing

the NV electron spin into the $|m_s = 0\rangle$ ground state, a resonant microwave pulse of length $\pi/2$ creates a superposition of the $|0\rangle$ and $|+1\rangle$ energy levels,

$$|\Psi\rangle = \frac{1}{\sqrt{2}}(|0\rangle + e^{i\phi}|1\rangle),$$

where the accumulated phase after precession time τ is $\phi = 2\pi\gamma B\tau$ where B is the amplitude of the magnetic field to be determined and $\gamma = g_s\mu_B/h = 2.8$ MHz/gauss the NV electron spin gyromagnetic ratio. Following the precession interval, a second $\pi/2$ MW pulse projects the spin back onto the quantization axis which is measured in the laboratory as a population difference between $|0\rangle$ and $|+1\rangle$, and read out optically through the spin dependent fluorescence of the NV center. Sensitivity is therefore improved by increasing the free precession time τ in order to maximize the accumulated phase, however, dipolar coupling to other magnetic impurities in the spin bath randomizes the accumulated phase after time T_2^* , the inhomogeneous NV dephasing time. Sensitivity in this scheme is optimized when the NV is allowed to precess in the magnetic field for $\tau \sim T_2^*$ and is given by

$$\eta_{ramsey} \sim \frac{\hbar}{g_s\mu_B} \frac{1}{C\sqrt{N\beta T_2^*}}.$$

For AC magnetometry, the Ramsey sequence can be modified by bisecting the free precession interval τ with a single resonant π pulse. The pulse is precisely timed to occur at the node of the oscillating field [Fig 1-3(b)] and deems to swap the accumulated phase from the $|1\rangle$ to the $|0\rangle$ state. For slow components of the external magnetic noise, the swap allows the second half of the free precession interval to compensate for phase randomization acquired during the first half of the interval. Using this sequence, τ can be increased to the homogeneous spin coherence time T_2 often orders of magnitude longer than T_2^* . The sensitivity for sensing an AC field is then improved when compared to sensing a DC field by a factor $\sqrt{T_2^*/T_2}$. This sequence is known as a Hahn-Echo sequence but AC magnetometry can also be performed by more complex dynamical decoupling techniques [9, 51].

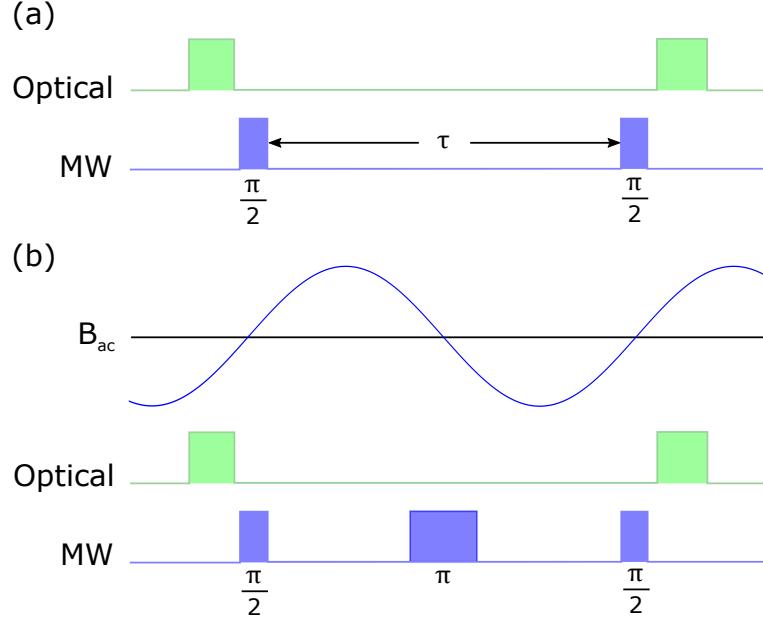


Figure 1-3: **Pulsed Magnetometry Sequences** **a)**) Ramsey Sequence for DC magnetometry **b)**) Hahn-Echo Sequence for AC magnetometry.

1.4 Rabi oscillations

When an on- or near-resonant MW pulse is applied to a ground state transition in the NV, e.g. $|0\rangle \rightarrow |+1\rangle$, the NV spin state population will oscillate coherently between these two levels at a rate called the Rabi frequency (Ω_R). This rate of oscillation is a function of the amplitude of the applied MW pulse. It is commonly measured by consecutively applying a polarizing laser pulse, a MW pulse, and a readout pulse [Fig. 1-4 (a)] and varying the MW pulse length after each iteration.

Fig. 1-4 (b) plots a typical Rabi curve and its decay envelope. If the NV is originally in $|0\rangle$ (ie. at time $t = 0$) and we let the system evolve, then the probability that the spin is found in $|+1\rangle$ is $P_{+1} = \left(\frac{\omega_1}{\Omega_R}\right)^2 \sin^2\left(\frac{\Omega_R t}{2}\right)$ where $\Omega_R = \sqrt{(\omega - \omega_0)^2 - \omega_1^2}$ is the Rabi frequency, ω is the radial frequency of the oscillating field $B_1(\omega)$, ω_0 the resonant frequency of the transition, and ω_1 the (max) Rabi frequency at zero detuning. At resonance, the driving frequency is $\omega = \omega_0$ and the transition probability becomes $P_{+1} = \sin^2\left(\frac{\omega_1 t}{2}\right)$. In order to therefore drive the entire population from e. g. $|0\rangle$ to $|+1\rangle$ as needed in, for example, the Hahn-Echo sequence described in 1.3.3, one needs to apply a pulse length such that $\sin^2\left(\frac{\omega_1 t}{2}\right) = 1$ which is satisfied when $t = \frac{\pi i}{\omega_1}$. For a

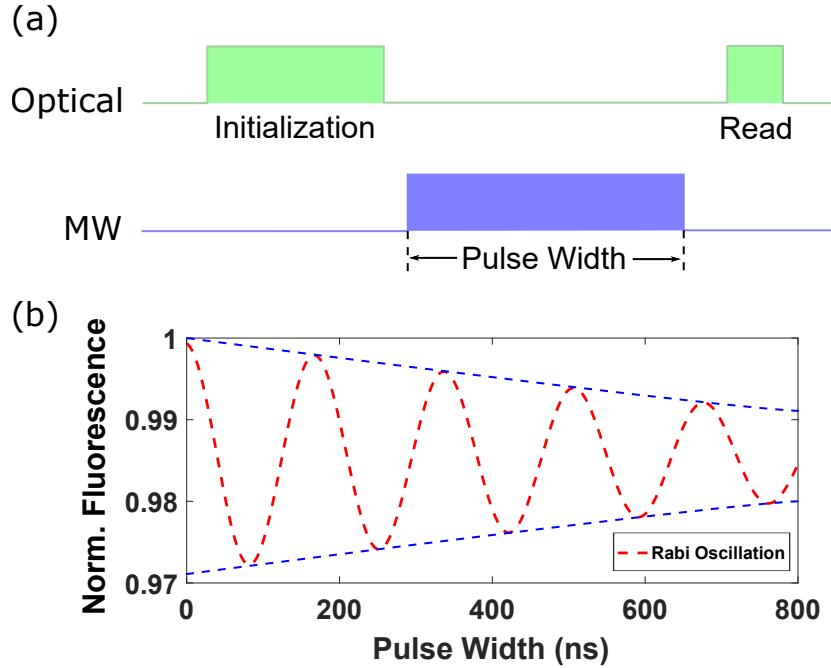


Figure 1-4: **Rabi pulse sequence and oscillations** **a)** Pulse sequence for detecting Rabi oscillation between two spin sublevels **b)** Example Rabi oscillations (—) with exponential decay envelope (—).

Ramsey-type sequence that requires an equal superposition between $|0\rangle$ and $|+1\rangle$ one needs to apply half the π pulse, $t = \frac{\pi}{2\omega_1}$. The Rabi oscillations however decay due to inhomogeneous broadening of the ensembles linewidth, and are therefore fit by the decaying envelope $\exp\{- (PW/T)^p\}$, where PW is the pulse width and T and p are fit parameters.

Chapter 2

The Loop Gap Resonator

As mentioned in the introduction, for many applied modalities within applications that use NV centers, the MW field (often denoted B_1 from NMR nomenclature), requires both high power and high uniformity to achieve high-fidelity quantum-state manipulation over the entire sample volume. As volumes are increased however, to maximize the number of NVs addressed without having a deleterious affect on the optimal measurement time, applying such a field becomes more difficult using standard approaches such as shorted coaxial loops [15, 13], microstrip waveguides [2, 35], and 50 Ω -terminated coaxial transmission lines [80, 52, 82, 81]. These broadband approaches allow arbitrary drive frequencies, however, the lack of resonant enhancement forces a compromise between the addressed volume and field strength. Section 2.1 describes how planar lumped-element resonators such as split-ring resonators [6], planar-ring resonators [82, 64], omega resonators [73, 36, 67], and patch antennas [82] can improve coupling between the resonator and the NVs by resonantly enhancing the local B_1 field and thus enable MW driving over larger regions, but at the expense of bandwidth and thus, for an operational magnetometer, dynamic range. Additionally, planar resonators are shown to yield poor homogeneity in the planes normal to their surface and therefore lend themselves less to bulk magnetometry than to 2D imaging applications. To address this shortcoming 3D resonators and cavities can be employed such as enclosed metallic cavity resonators [63], enclosed dielectric resonators [8, 44, 17], open dielectric resonators [40], and three-dimensional lumped element res-

onators [3], which provide good field homogeneity and strong resonantly enhanced fields, but offer little to no optical access. Since all-optical initialization and readout is a primary benefit for many solid-state spin systems, including NV diamond [21], such a trade-off is incompatible with many existing and envisioned applications [65].

To address this current shortcoming a three-dimensional tunable loop-gap resonator (LGR), based on the anode block of a cavity magnetron, is used to achieve desired MW drive strengths homogeneously over large areas. Additionally, its open geometry allows for good optical accessibility for interrogation volumes centered within the LGR cavity. Traditionally, the LGR has been used either as the anode block of cavity magnetrons [16], or as a low frequency (2-4 GHz) lumped element resonator for electron paramagnetic resonance (EPR) studies [61].

2.1 Resonant Enhancement of the MW field

The LGR acts classically like an underdamped oscillator. It stores MWs within the confines of its geometrical structure by allowing the energy to oscillate back and forth between an electric and magnetic potential. At resonance (ω_0) the ratio of magnetic energy to electric energy is 1. The time τ_{ring} the energy can oscillate before its power is reduced by a factor of $1/e$ is characterized by a dimensionless quantity called the Q-factor. It's defined by the following ratio

$$Q = \omega_0 \frac{\text{StoredEnergy}}{\text{PowerLoss}}. \quad (2.1)$$

If the resonator is therefore continuously fed by an external power source an enhancement of the stored energy takes place that is proportional to the Q-factor of the cavity. The magnitude of the magnetic flux within the center cavity (for a cylindrical resonator) is given by

$$|B_1| \approx 2 \left[\frac{\mu_0}{\omega V_r} \right]^{1/2} \cdot \sqrt{P_0} \cdot \sqrt{Q}, \quad (2.2)$$

where μ_0 is the vacuum permeability, P_0 is the power coupled to the resonator, ω is the angular frequency, and V_r is the volume of the center loop. It's therefore clear

that a resonant enhancement of the magnetic field amplitude is induced which is proportional to the square root of the Q-factor.

2.2 Model

The following sections build a model of the LGR both as an equivalent circuit and as solutions to Maxwell's equations for the LGR's geometry. Figure 2-1 shows the LGR with geometrical parameters used in the following sections. The focus here lies on hole-and-slot type LGR resonators since this variation is designed and used in the rest of this thesis. Other types of resonators are shown in section 2.3 Figure 2-3.

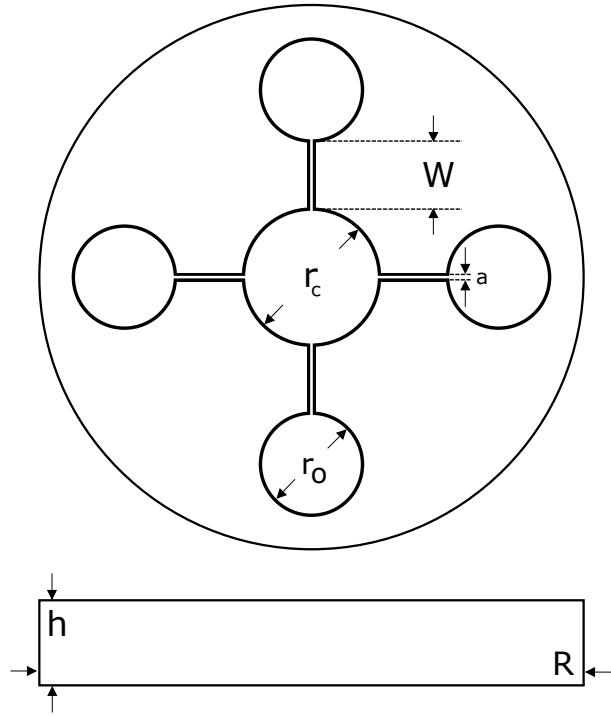


Figure 2-1: **LGR dimensions** Geometrical parameters of LGR used in sections 2.2.1 and 2.2.2

2.2.1 Equivalent circuit picture

The LGR can be modeled by an equivalent circuit in which the gaps behave like capacitors and the loops like inductors. It's important to note that such a picture neglects effects such as radiation losses or fringing fields that extend into space above

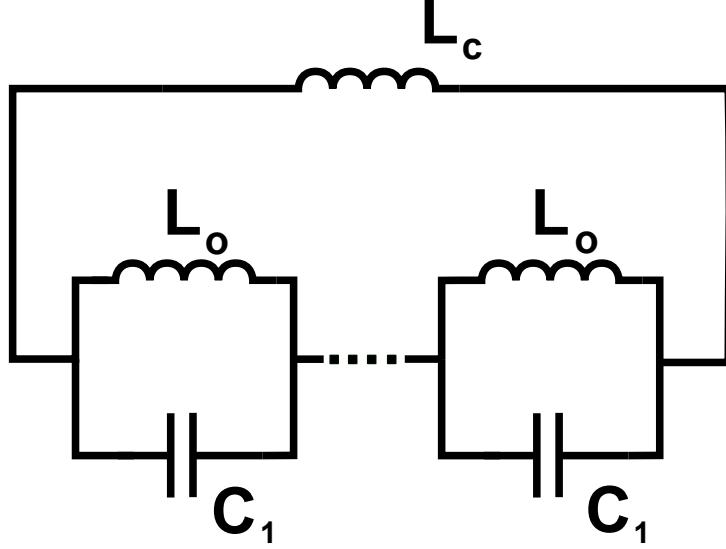


Figure 2-2: **LGR equivalent circuit diagram** Diagram showing equivalent inductance and capacitance of LGR and their connections.

and below the LGR. However these effects can be incorporated with considerable effort and are described in detail within the following references [49, 61, 78]. For an m loop and n gapped LGR, the equivalent circuit is depicted in Figure 2-2. Using the variables given in Figure 2-1, the charge at the gap walls creates a capacitance C_1 , and circulating currents around each loop create an inductance L_1

$$C_1 \approx \frac{\epsilon_r \epsilon_0 W h}{a}, \quad L_1 \approx \frac{\mu_0 \pi r_i^2}{h}, \quad (2.3)$$

where r_i is the radius of either loop ($i \equiv o, c$). Using circuit analysis we can solve the diagram in Figure 2-2 for the total capacitance, C ,

$$C = \frac{C_1}{n}, \quad (2.4)$$

and total inductance, L ,

$$L = \frac{n L_o L_i}{n L_o + L_i}. \quad (2.5)$$

The resonant frequency of the LGR is therefore given by

$$f_0 = \frac{1}{2\pi\sqrt{LC}} \quad (2.6)$$

2.2.2 Solution to Maxwell's equations

The full derivation of the solutions to Maxwell's equations for an n gap LGR can be found in references [59, 48, 50]. However, this section is intended to give a brief overview of the solutions, how they are attained, and how they can be used to estimate the field homogeneity and strength for an n gap LGR. In general, Maxwell's equations for the LGR center cavity can be solved by using Bessel and Neumann functions which are generally found to be the solutions to finite length cylindrical waveguides [29]. Neumann functions however are singular at the origin and therefore only Bessel functions (of the first kind) need to be considered. The magnetic field solution then takes the form

$$B_z^{(p)} = \mathcal{J}_p(k\rho)e^{ip\phi}. \quad (2.7)$$

Where we are operating in cylindrical coordinates and \mathcal{J}_p is the p^{th} order Bessel function and $k = \omega\sqrt{\mu_0\epsilon_0}$. If we assume that the field in the center loop is fully directed in z then the magnetic field is simply

$$B_z = B_z(\rho, \phi)e^{i\omega t}, \quad B_\rho = B_\phi = 0. \quad (2.8)$$

The periodic boundary condition for the electric field is

$$\begin{aligned} E_\phi &= 0 \quad \text{at} \quad \rho = r_c \\ &\quad \text{for } 2N\pi/n + \delta/2 \leq \phi \leq 2(N+1)\pi/n - \delta/2, \end{aligned} \quad (2.9)$$

and

$$\begin{aligned} E_\phi &= E \quad \text{at} \quad \rho = r_c \\ &\quad \text{for } 2N\pi/n - \delta/2 \leq \phi \leq 2(N+1)\pi/n + \delta/2, \end{aligned} \quad (2.10)$$

where N is an integer, n is the number of gaps, and δ is the arc angle that is swept out by the capacitive gap, in radians. Additionally we know from Maxwell's equations that

$$E_\rho = -i\frac{c\mu_0}{k\rho}\frac{\partial B_z}{\partial\phi}, \quad (2.11)$$

$$E_\phi = i \frac{c\mu_0}{k} \frac{\partial B_z}{\partial \rho}. \quad (2.12)$$

Using equation 2.7 in 2.11 and 2.12 and solving for the appropriate Bessel functions using the boundary conditions 2.9 and 2.10 yields, for the magnetic field only,

$$|B_z(\rho, \phi)| = -c\epsilon\mu_0 \frac{nE\delta}{2\pi} \times \left(\frac{\mathcal{J}_0(k\rho)}{\mathcal{J}_0(kr_c)} + 2 \sum_{p=1}^{\infty} \frac{\mathcal{J}_{np}(k\rho)}{\mathcal{J}_{np}(kr_c)} \frac{\sin(np\delta/2)}{np\delta/2} \cos(np\phi) \right), \quad (2.13)$$

Where E is the maximum field contained in the capacitive gap [Figure 2-9], and $\epsilon = \epsilon_r \epsilon_0$. In this case ϵ_r is given by the shim material used to tune the resonator (assuming it fully spans the width of the gap). To get an estimate of the field deviation between the maximum and minimum points we should examine the center and boundary cases (ie. $\rho = r_c$ and $\rho = 0$). At the cavity center we find,

$$|B_z(0, 0)| \approx c\epsilon\mu_0 \frac{nE\delta}{\pi kr_c} \quad (2.14)$$

and at the cavity sidewalls (choosing $\phi = 0$ for convenience),

$$|B_z(r_c, 0)| \approx -c\epsilon\mu_0 \frac{nE\delta}{\pi} \left(-\frac{1}{kr_c} + \frac{kr_c}{n} (1 - \ln n\delta/2) \right). \quad (2.15)$$

To quantify the inhomogeneity we use the peak to peak variation σ_{pp} defined as,

$$\begin{aligned} \sigma_{pp} &= 2 \frac{|B_z(0, 0)| - |B_z(r_c, 0)|}{|B_z(0, 0)| + |B_z(r_c, 0)|} \\ &\approx 2 \frac{(kr_c)^2}{n} (1 - \ln n\delta/2) \end{aligned} \quad (2.16)$$

For the LGR used in this study (introduced and described in more detail in the sections to come) we can calculate $\sigma_{pp} \approx 8.9\%$ across the entire center loop when excited at 2.87 GHz. We will see in sections 3.2 and 3.3 that this estimate is too low. This is likely due to the fact that the model described above neglects fringing field effects and thus assumes that the electric field has no axial variation and that the magnetic field is perfectly polarized in the z-direction. Furthermore, using equation 2.14 and the electric field information contained in figure 2-9 we calculate the estimated field

strength in the cavity center to be $B_z(0,0) \approx 2.2$ gauss which, referring to section 3.2 and 3.4, is too low an estimate. This most likely arises from the fact that the model above neglects any resonant enhancement of the field due to the cavity Q factor (see section 2.1).

2.3 LGR Design

Due to the loop gap resonator's existence since the early 20th century [16] it has seen many variations and modifications all designed with particular applications in mind. Figure 2-3 shows the cross section of a variety of LGRs including rising-sun, vane, slot, and hole-and-slot type resonators. EPR experiments at low frequencies (2-4 GHz) quickly adopted the LGR as opposed to more traditional TE_{102} type cavities because of the LGR's smaller size relative to the frequency of excitation. At 3 GHz the side length of the TE_{102} cavity must be at least 5 cm which drastically reduces the cavity filling factor for small samples—a parameter necessary for the sensitivity of an EPR signal. Since many aspects of EPR spectroscopy are mirrored in NV magnetometry (requirement of homogeneous and strong microwave signals, frequency of operation, etc.) we selected to design a hole-and-slot type resonator.

2.3.1 LGR

A standard hole-and-slot LGR with n outer loops can be approximated as n coupled LC resonators oscillating in tandem at a target resonant frequency [78]. Circulating currents around the central and outer loops create a total inductance 2.5, and charge at the gaps creates the total capacitance 2.4 as found in section 2.2.1. In practice, the central loop diameter is set to $\sim 5 - 10$ mm, corresponding to the typical size of a diamond plate. The outer loop diameters are chosen to match the inner diameters within a small factor to ensure return flux is captured and does not extend into the annular region around the LGR [49]. Since the outer and inner loops set the effective inductance of the resonator, the gap area $A = h \times W$ is constrained by the dual LGR

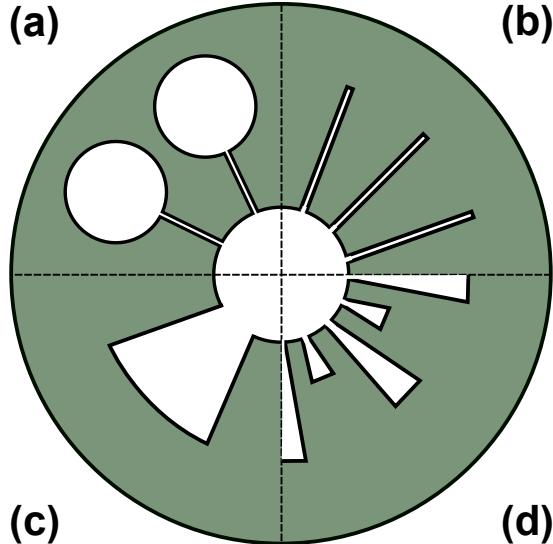


Figure 2-3: **Loop Gap Resonator Variations** **a)** Hole and Slot. **b)** Slot. **c)** Vane. **d)** Rising Sun - type

design objectives of (i) maintaining optical accessibility, which limits the thickness of the device, and (ii) bounding f_0 above the target resonant frequency in order to allow for further tuning via dielectric shims (discussed in section 2.3.2). Additionally, while increasing the number n of loops and gaps can improve B_1 uniformity (see equation 2.16) and lower the LGR's resonant frequency, this approach results in a denser mode spectrum [26] and increases the likelihood of cross-mode excitations deleteriously altering the field distribution within the central loop. As a compromise, the design employs $n = 4$ outer loops [Fig. 2-4 (a)] allowing for sufficient uniformity while locating the closest eigenmode more than 2 GHz below the TE_{10} eigenmode [Table 2.3.1].

The LGR in this work therefore consists of a central loop with radius $r_c = 4$ mm surrounded by four symmetrically arranged outer loops of radius $r_o = 3$ mm as shown in Figure 2-4 (b). The outer loops return magnetic flux to the central loop and therefore oscillate antisymmetrically with the central loop (π out of phase). The side walls of the capacitive gaps are separated by $d = 254$ μm . With these dimensions, using equations 2.3, 2.5, and 2.4 yield $L = 8.7$ nH and $C = 0.17$ pF, resulting in an expected resonant frequency for the naked air-gapped LGR of $f_0 = 4.1$ GHz, approximately 1.2 GHz above the NV resonance frequencies. An eigenfrequency simulation of the

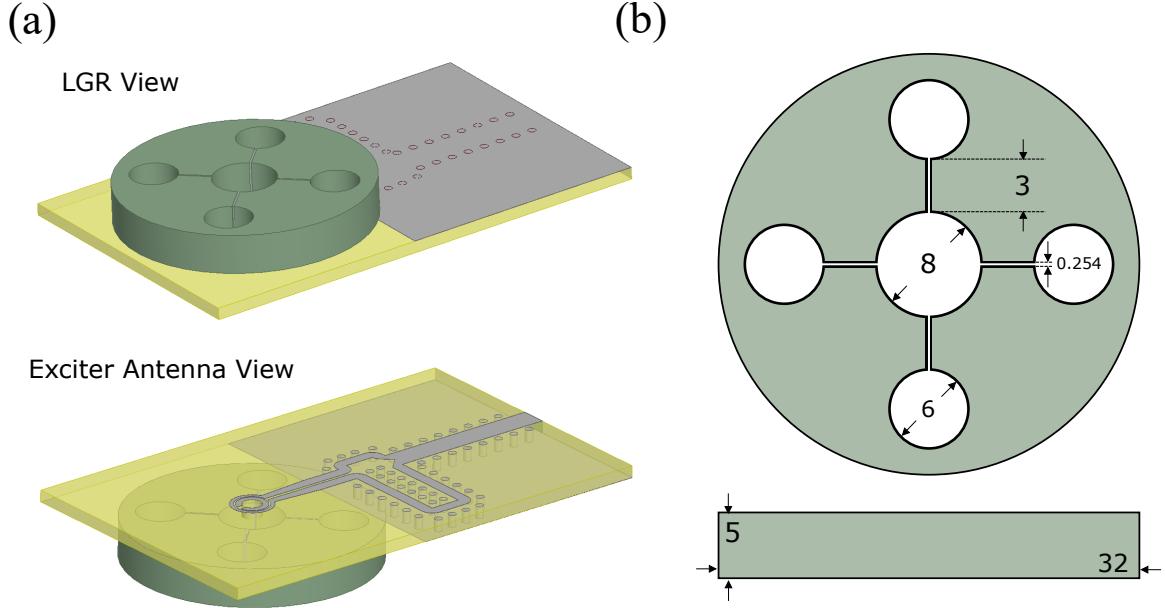


Figure 2-4: Rendering and Wire Diagram of Loop Gap Resonator **a)** The metallic resonator employs a five-loop four-gap architecture. Microwaves are coupled into the LGR via the exciter antenna, which is fabricated on a printed circuit board. **b)** Line drawing of the LGR. All dimensions are in mm. Optional mounting holes and radial access port for laser excitation are now shown.

resonator using the geometrical parameters listed above was completed in ANSYS HFSS and the distribution of the magnetic flux density (B_1) for the TE_{10} mode is depicted in Figure 2-5. As mentioned above, for this mode the center loop oscillates π radians out of phase with the outer loops. For the air-gapped resonator, HFSS returns a real eigenfrequency at 4.57 GHz (depicted in Figure 2-5 and Table 2.3.1)

The LGR is fabricated via wire electron discharge machining, which is well-suited for producing the tight tolerances and vertical side walls required for the narrow $d = 254\mu\text{m}$ capacitive gaps. A titanium alloy (Ti-6Al-4V) was chosen as the resonator cavity material. The lower conductivity of this alloy compared to that of copper ($\sigma_{Ti} = 5.8 \times 10^5 \text{ S/m}$ vs. $\sigma_c = 59 \times 10^6 \text{ S/m}$) allows for a broader resonance with a 3dB bandwidth $\Delta_{3dB} = 80 \text{ MHz}$, sufficient to address all eight NV resonances for bias magnetic fields B_0 up to ~ 20 gauss. This 80 MHz bandwidth corresponds to a loaded quality factor $Q_L \equiv f_0/\Delta_{3dB} \approx 36$ when the LGR is critically coupled to the driving source (see section 3.1). The LGR may be optionally fit with a radial access hole (for laser excitation of the NV ensemble) and three # 2-56 mounting holes, which

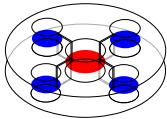
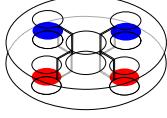
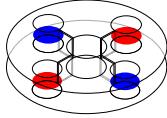
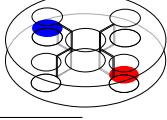
Mode	freq. sim.(GHz)	freq. meas.(GHz)	figure
1 (TE_{10})	4.6	4.66	
2	2.3	2.53	
3	2.33	2.51	
4	~ 2	1	

Table 2.1: Some modes the LGR supports and their measured vs. simulated frequencies. Many separate modes are degenerate due to their symmetrical nature. Additionally

affix the LGR to an exciter antenna, discussed next.

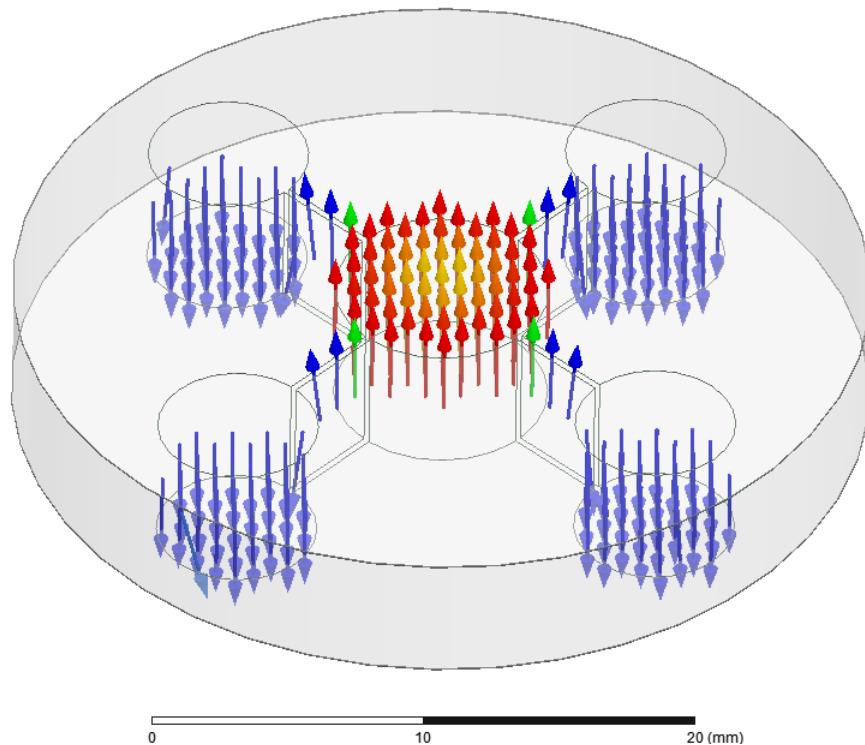


Figure 2-5: **Eigenfrequency solution to LGR** TE_{10} mode located at $f_0 \approx 4.6$ GHz. The outer loops are oscillating π radians out of phase with center loop.

2.3.2 Tuning

The LGR resonant frequency f_0 is additionally tuned by inserting and translating dielectric shims in the LGR's capacitive gaps, thereby increasing total capacitance C until f_0 overlaps the NV resonance frequencies as desired. Shimming material should be chosen to provide a high dielectric (and thus large tuning range) and low loss tangent ($\tan \delta$, where δ is the inverse skin-depth). We employ 200 μm thick C-plane sapphire, which is commercially available in semiconductor grade 50.8 mm diameter wafers, can be cut on standard wafer dicing saws, has a high relative permittivity of $\epsilon_r = 11$ parallel to the C-plane [75], and exhibits a low dielectric loss of $\tan \delta < 0.0001$ at 3 GHz [75, 33]. The sapphire shims are cut to lengths longer than the $l_c = 4$ mm radial length of the capacitive gaps, wedged into the gaps, and held in place with PTFE thread tape. These sapphire shims are then translated radially until the desired value of f_0 is attained. The shims are always positioned so that excess shim length extends into the outer rather than the central loop, in order to minimally perturb the central loop B_1 field. Simulations further suggest that radially symmetric shim configurations produce the best B_1 field homogeneity, as asymmetries in shim placement perturb the desired TE_{01} field distribution.

2.3.3 Excitation Design

To couple MW power into the LGR we utilized two separate methods, each to be used for different NV applications. For magnetic microscopy, complete 2π steradian optical access to the center cavity is of the utmost importance. For such modalities lateral coupling using a shorted coaxial loop [Figure 2-6 (a)] can be used to minimize the blocking of optical access to the central loop [43]. Using this method, resonator coupling is modified by changing the coaxial loop position in z relative to the LGR. In this way the LGR can be quickly and effectively critically coupled for any shim configuration (ie. resonant frequency) [Figure 2-6 (b)]. Note that changing the coupling loop distance affects the mutual inductance between the shorted-loop and the resonator. As an undesired consequence, the resonant frequency of the total device

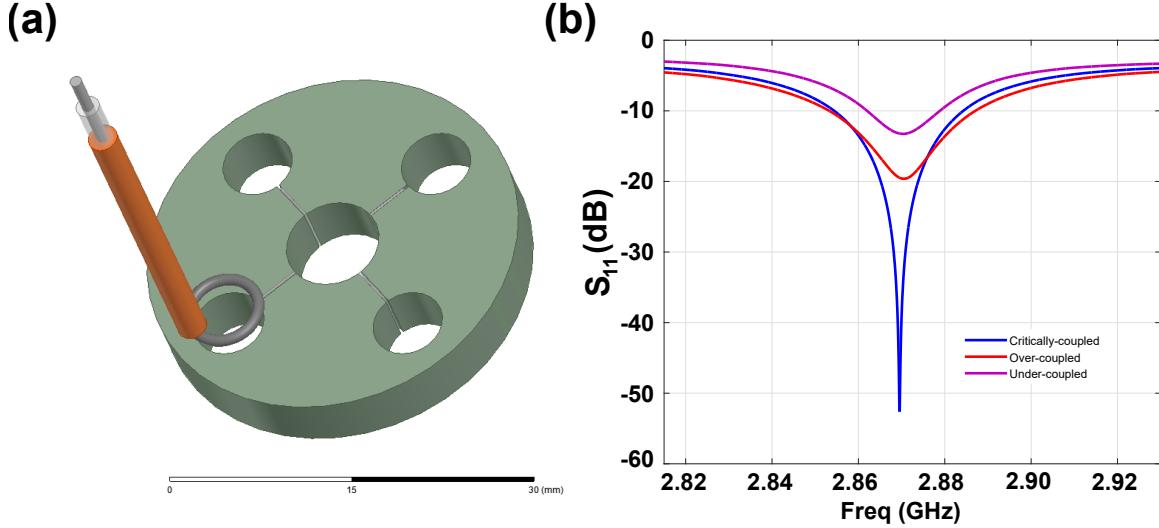


Figure 2-6: **3D Rendering of coupling loop and scattering parameter for different coupling configurations** a) Rendering of lateral coupling loop and LGR. b) Scattering parameter S_{11} for different coupling configurations. Critically coupled (—) at $z \approx 1$ mm, under-coupled (—) at $z \approx 1.25$ mm, over-coupled (—).

shifts away from the frequency it was initially tuned to. A simple optimization process however, between shim placement and loop/LGR distance, can lead to the desired coupling at the targeted frequency.

The purpose of the second devised coupling method is to provide a mechanically stable and wide bandwidth match for a future field-able NV magnetometer. While the lateral-loop coupling approach yields near perfect optical access to a sample placed in the center loop of the LGR, the long lever arm of the coaxial cable is susceptible to perturbation in a non-laboratory setting. An oscillation in the coupling loop manifests itself in an oscillation in the value of the coupling parameter β and, in effect, an oscillation of the LGR resonant frequency and MWs supplied to the NVs. For applications that can sacrifice optical access, such as a bulk field-able magnetometer, we design a split-ring coupling structure on a dielectric substrate which is subsequently mounted on the LGR [Figure 2-4 (a)]. The fixed distance between the split-ring and LGR prevents quick "on-the-fly" coupling when the device is shim-tuned to another resonant frequency. Therefore the device must be well coupled across a wide bandwidth, which can be achieved using a balun (**balanced-unbalanced**) placed between the feed-line and the exciter antenna (split-ring resonator). Figure 2-7 shows the exciter board

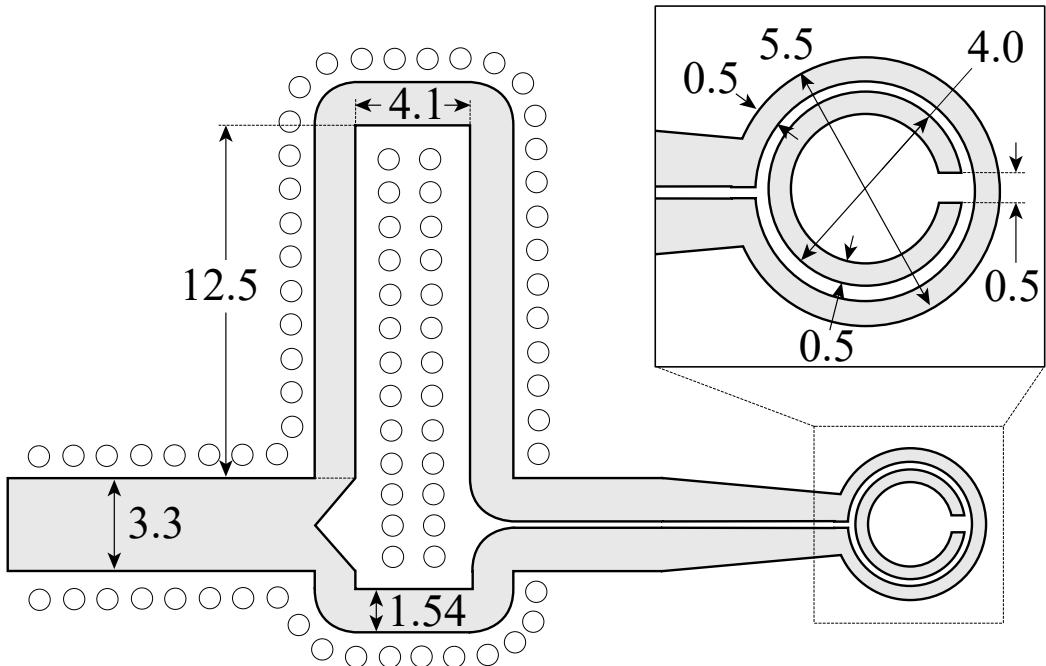


Figure 2-7: Exciter board drawing A feedline, 50:50 power splitter, and balun (**balanced unbalanced**) feed the split ring resonator, which is coupled to the LGR. All dimensions are in mm. Optional mounting holes and radial access port for laser excitation are not shown

composed of a 50:50 power splitter, a balun and a split-ring resonator. The balun is designed to match the exciter antenna to the LGR over a minimum bandwidth of 1 GHz centered at the zero-field splitting of the NV (D_{gs}). The 2D electromagnetic simulation tool Sonnet was used to ensure a flat S_{21} and S_{31} response between the feed-line and split-ring exciter antenna over the frequency range in question.

Differential driving of the balun mitigates common-mode noise on the two traces, which might otherwise couple to the split-ring resonator. A via shield along a portion of the balun helps reduce interference and cross-talk between traces, controls trace impedance, and reduces radiative losses along the balun's π phase delay arm. The exciter antenna is fabricated from a 1oz. copper trace with immersion silver finish on a 1.524 mm thick dielectric substrate (Rogers RO4350B). Although the proximity of the split-ring resonator perturbs the field distribution inside the LGR, both simulations and measurements suggest this effect is minimal and not the dominant source of inhomogeneity (See section 3.3).

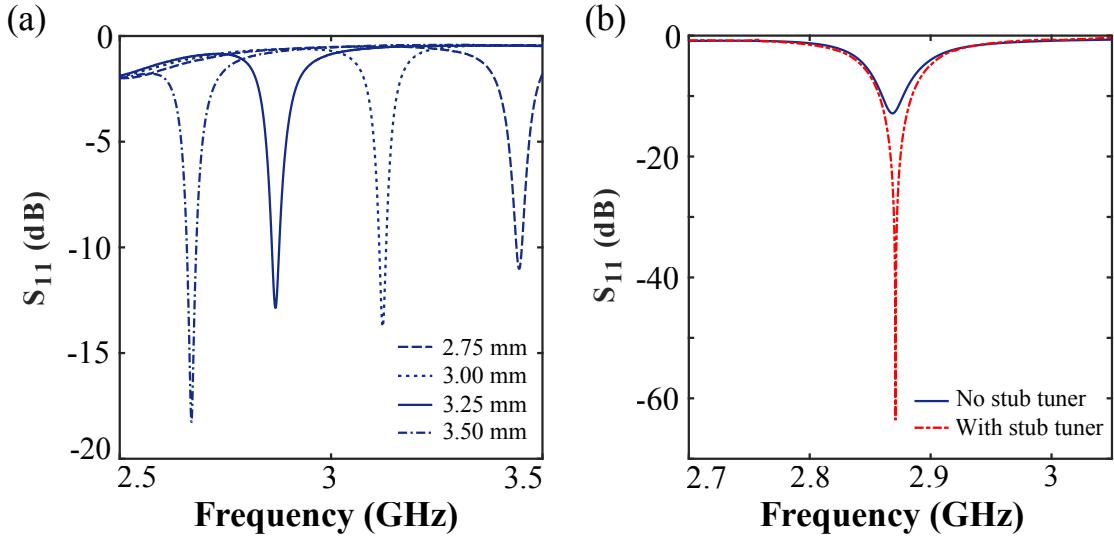


Figure 2-8: Frequency tuning and impedance matching of LGR composite device. (a) The resonant frequency f_0 is adjusted by translating the sapphire shims in the four capacitive gaps. In the absence of a stub tuner, the LGR composite device exhibits S_{11} values between -10 and -20 dB from 2.5 to 3.5 GHz, indicating at least $\gtrsim 90\%$ of power delivered to the LGR composite device contributes to B_1 in this range. (b) Nearly perfect critical coupling can be achieved with a stub tuner, allowing practically all incident MW power to contribute to B_1 .

Although the microstrip balun is designed to match the feed-line and the split ring component of the exciter antenna at frequencies near 2.87 GHz, good matching is achieved from 2.5 GHz to 3.5 GHz as well. For drive frequencies between 2.5 and 3.5 GHz, the exciter antenna board couples more than 90% of incident MW power into the LGR, as shown in Figure 2-8 (a). For a specific fixed frequency, the impedance matching may be further optimized by inserting a stub tuner between the MW source and the exciter antenna board, as shown in Figure 2-8 (b). The stub tuner changes the effective electrical length of the exciter circuit and therefore modifies the coupling between the split ring resonator and the LGR. Similar matching can be achieved using a varactor diode instead of a stub tuner.

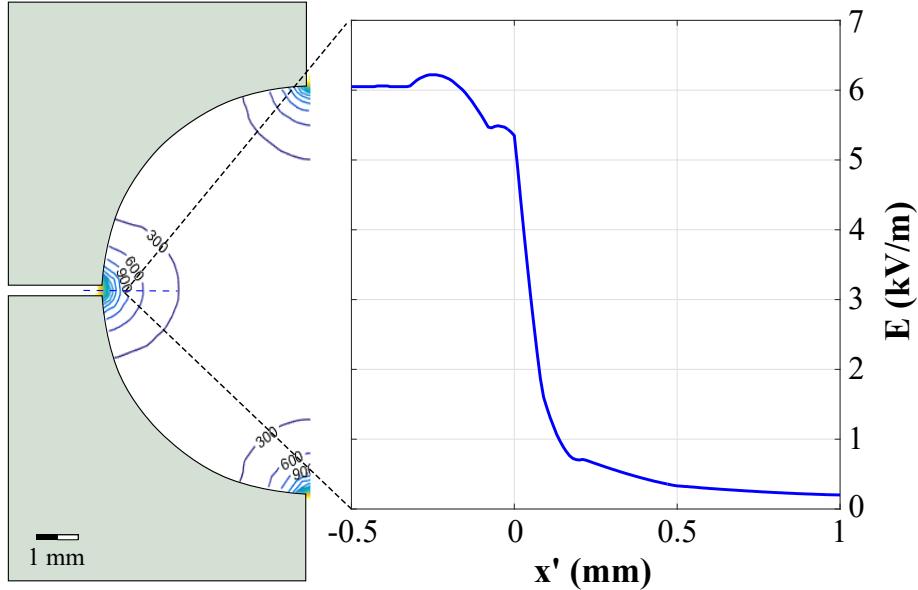


Figure 2-9: **Simulated electric field magnitude E in vicinity of LGR capacitive gap.** Inset depicts the electric field magnitude E as a function of distance from the capacitive gap with $x' = 0$ mm corresponding to the plane of the central loop-gap interface.

2.4 Electric Field

One challenge that many MW solutions face is maintaining good coupling and a steady resonant frequency when a sample is introduced. For example, if a dielectric sample is placed on a planar resonator the dramatic change in capacitance between trace elements causes a shift in the resonant frequency [6, 64, 82] of the oscillator. Just like planar fabricated resonators, the LGR is a lumped element device but its large size permits an improved spatial separation between the electric and magnetic fields in the cavity. The electric field in the TE_{10} mode is confined to the capacitive gaps and thus has little interaction with a dielectric sample placed in the center cavity. In practice, fringing electric Fields from the capacitive gaps extend partially into the LGR's central loop as shown in Figure 2-9. However, at distances > 1 mm from the capacitive gaps, the electric Field magnitude $|E|$ is decreased by >10 x from the peak Field inside the capacitive gap. Consequently, insertion of a diamond (with $\epsilon_r \approx 5.7$ at 3 GHz [37]) beyond this region has little if any effect on the LGR resonant frequency f_0 .

Chapter 3

LGR Performance and Field Characterization

In this chapter the LGR electrical and magnetic are discussed and measured. All simulations were completed in ANSYS HFSS a full-wave electromagnetic simulation tool.

3.1 Quality Factor

As mentioned in section 2.1, The quality (or Q) factor of an oscillator quantifies how often (in terms of the oscillation period) the energy will oscillate back and forth until its initial amplitude is reduced by a factor of $1/e$. At critical coupling ($\beta = 1$) the intrinsic Q (Q_0) of the resonator (which quantifies the oscillation lifetime due to resistive losses) is calculated as the inverse of its fractional bandwidth (FBW),

$$Q_0 = \frac{1}{FBW} = \frac{f_0}{\Delta_{3dB}}. \quad (3.1)$$

The fractional bandwidth however is calculated from the loaded Q (Q_L) which takes into account coupling losses due to power reflection at the exciter antenna/LGR interface. Incorporating these reflections is achieved by assigning an external Q (Q_e)

to account for these losses. Q_e then combines with Q_0 in a parallel configuration

$$\frac{1}{Q_L} = \frac{1}{Q_0} + \frac{1}{Q_e}, \quad (3.2)$$

to yield Q_L . The intrinsic Q, Q_0 , and the external Q, Q_e , characterise the most dominant loss mechanisms of the device. Other loss mechanisms and their contribution to Q_L are discussed in reference [59]; they include, but are not limited to, loss in a sample, radiation losses, surface wave losses, hand-shaking (if not properly shielded), etc..

Since the quality factor is inversely proportional to the resonator bandwidth the LGR needs to exhibit fairly low Q in order to address all eight NV resonances and their shifts due to an external field. The LGR was thus designed to accommodate an NV ensemble that has been split using an up-to 14 gauss biasing field B_0 . Since the NV gyromagnetic ratio (γ_B) is 2.8 MHz/gauss, this corresponds to an ideal bandwidth of 78 MHz and, at 2.87 GHz, a Q of ~ 36 . In addition to a wide dynamic range, a low Q allows for the use of concatenated pulse sequences without employing additional methods to evacuate power from the resonator before the next pulse is applied (e.g. active cancellation).

3.1.1 Ringdown time

As mentioned above, in order to apply concatenated MW pulses to a sample in the LGR (as is done often in NMR and NV applications [76, 9]) the power oscillating in the cavity must be evacuated or dissipated in between pulses. One method used is to apply active cancellation techniques that either introduce extra components to the excitation circuitry to abruptly de-tune the resonator before the next pulse is applied [54] or apply a secondary pulse that is designed to destructively interfere with the cavity ring-down [25]. Another, and also the technique applied here, is to make the resonator intrinsically lossy and therefore dissipate the left-over power in the cavity as either heat or radiation. To calculate the ring-down time τ_{ring} of the LGR we apply a damping exponential to the field within the cavity such that $B(t) = B_{init}e^{-\pi f_0 t/Q}$

(neglecting any phase caused by a shift in the resonant frequency), and solving for the time t at which the amplitude has decreased to $1/e \cdot B_{init}$. Doing this yields

$$\tau_{ring} = \frac{Q}{\pi f_0}. \quad (3.3)$$

Using equation 3.3 and the bandwidth and center frequency extracted from the measured data in Figure 2-8, one calculates $\tau_{ring} = 4$ ns which is sufficient for standard NV and NMR pulsed protocols [68, 38, 70].

3.2 Simulating the Magnetic Field

The B_1 field distribution in the center loop of the LGR was simulated using the full-wave electromagnetics simulation suite ANSYS HFSS. The simulation includes the 200 μm dielectric shims and the full exciter circuit depicted in Figures 2-7 and 2-4. The solution type was set to "driven modal" since the exciter board has a single trace interconnect and thus requires the solution of TE and TM propagation modes. Figure 3-1 shows the B_1 distribution computed by HFSS at an input power of 42 dBm. The exciter board (which extends over the LGR center loop along the line $x = y$ in the figure) clearly imparts a small perturbation on the otherwise radially symmetric field. The simulation predicts $B_1 \approx 4.8$ gauss at the LGR center and a maximum field of $B_1 \approx 5.4$ gauss at the perimeter. Two metrics are used to quantitatively characterize 2D regions of homogeneity, the fractional root-mean-square inhomogeneity σ_{rms} calculated as

$$\sigma_{rms} = \sqrt{\frac{\sum_{i=1}^N |B_{1,i}|^2}{N}} \cdot \mu_N^{-1}, \quad (3.4)$$

where i is an index over all B_1 field values in the region, N is the total number of values, and μ_N is the mean of all N values, and the fractional peak-to-peak variation σ_{pp} calculated as

$$\sigma_{pp} = \frac{[B_1^{max} - B_1^{min}]}{\mu_N}. \quad (3.5)$$

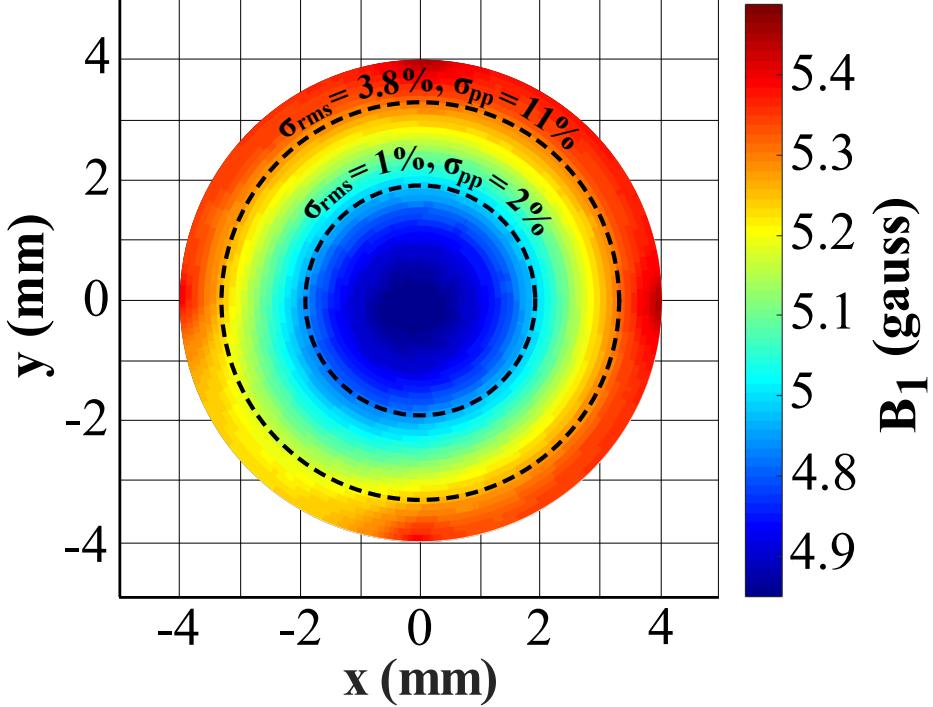


Figure 3-1: **Simulated magnetic field** Top-down cross section of center loop of LGR. Slice is taken at half height h . Simulations suggest the B_1 field distribution should be approximately radially symmetric, with the leading order deviation resulting from the exciter antenna. Dashed lines indicate the 32 mm^2 and 11 mm^2 areas within which the B_1 field uniformity is evaluated.

The use of both metrics facilitates comparison with alternative existing designs. Within a 32 mm^2 circular area centered in the LGR central loop, simulations indicate $\sigma_{rms} = 3.8\%$ and $\sigma_{pp} = 11\%$, whereas in a smaller 11 mm^2 circular area, simulations indicate $\sigma_{rms} = 1\%$ and $\sigma_{pp} = 2\%$.

As a three dimensional cavity resonator, the LGR provides better axial field uniformity than planar-only geometries [44, 40, 3]. Figure 3-2 plots the simulated B_1 along the LGR's symmetry axis, illustrating the improved axial field uniformity possible with three-dimensional cavity resonators, compared to that of planar-only geometries. The presence of the split ring resonator at $z = 4.024 \text{ mm}$ perturbs B_1 inside the LGR, shifting the point of maximal B_1 down by 0.4 mm, away from the split-ring resonator. Within a cylindrical volume of 3.14 mm^3 (1 mm radius and 1 mm thickness), centered around the point of maximal B_1 , the simulations predict $\sigma_{rms} = 0.78\%$ and $\sigma_{pp} = 3.7\%$. For a larger cylindrical volume of 12.6 mm^3 (2 mm radius and 1 mm

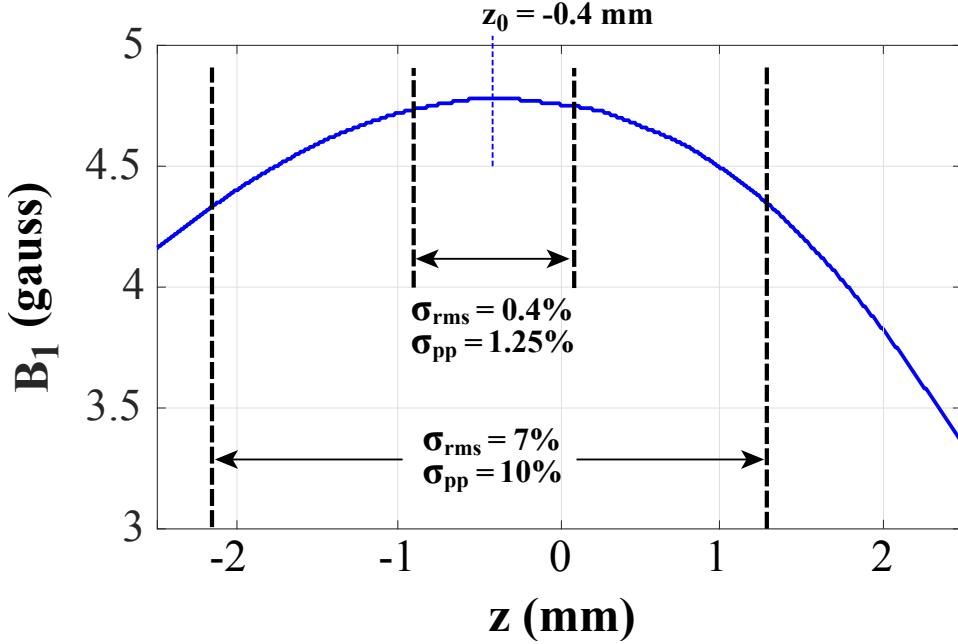


Figure 3-2: **Simulated B_1 field along LGR symmetry axis.** The symmetry plane of the LGR is located at $z = 0$ mm. The edges of the LGR are at $z = \pm 2.5$ mm, and the split-ring resonator is located at $z = 4.024$ mm. The presence of the split-ring resonator shifts the point of maximal B_1 off-center to $z_0 = -0.4$ mm.

thickness), the simulation predicts $\sigma_{rms} = 2\%$ and $\sigma_{pp} = 8\%$. These dimensions are comparable to those of commercially available single-crystal diamonds. Additionally, Figure 3-2 gives 1D regions of homogeneity along the LGR symmetry axis.

3.3 Measuring the Magnetic Field

Measuring the magnetic field distribution within the central loop of the LGR can be done in several ways. The simplest is to raster scan a magnetic probe across the cross section to be measured. However there are many drawbacks to this method. First, the spatial resolution is set by the size of the probe tip. Figure 3-3 shows the normalized magnetic field distribution of the LGR, measured by a 100B Beehive magnetic probe. The shielded loop diameter of the probe is 1 mm and thus the resolution is poor. Second, the probe has very little access to the center of the cavity. The data in Figure 3-3 was, for example, taken 1 mm above the LGR center loop; a region in which the magnetic field is highly divergent. Since the magnetic loop only

measures the component of the field that lies parallel with its central axis this provides a limited picture of the total field distribution. Finally, the proximity of the probe to the LGR perturbs the field and thus the distribution measured is an altered version of the field in the unperturbed scenario.

Another method—with similar drawbacks—is to measure the cavity transmission characteristics under intentional perturbation by a metal probe tip. By moving the perturbing probe tip, the transmission parameter S_{21} (when an out-coupler loop is placed into one of the lateral loops) changes proportional to the field at the point of measurement. Thus, if the metal tip is scanned across the cavity, a picture of the field distribution can be extracted.

Since the LGR in this thesis is designed to supply MWs to NV centers, one can utilize NV centers to, in turn, measure the strength of the supplied MWs. If the period of the Rabi frequency (as described in section 1.4) can be determined, then one can, using a simple relation, calculate the magnitude of B_1 (section 3.3.2 equation 3.8). This measurement of the field does not suffer from the drawbacks of the other two mentioned above and thus, it's the method employed in this thesis. The following subsections describe the measurement apparatus, measurement process, and calculations used to infer the strength of the B_1 field at various points within the LGR center loop.

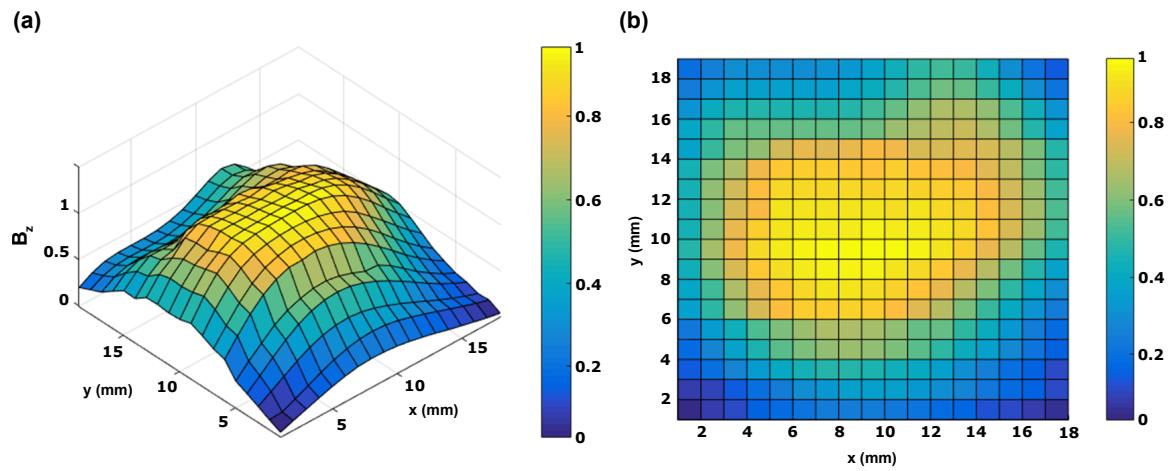


Figure 3-3: B_z component of field measured with probe **a)** 3D surface plot of B_z field distribution using a Beehive 100B magnetic field probe. Color bar units are normalized magnetic field. Normalized to their maximum value. **b)** Same data as in a) but top-down view.

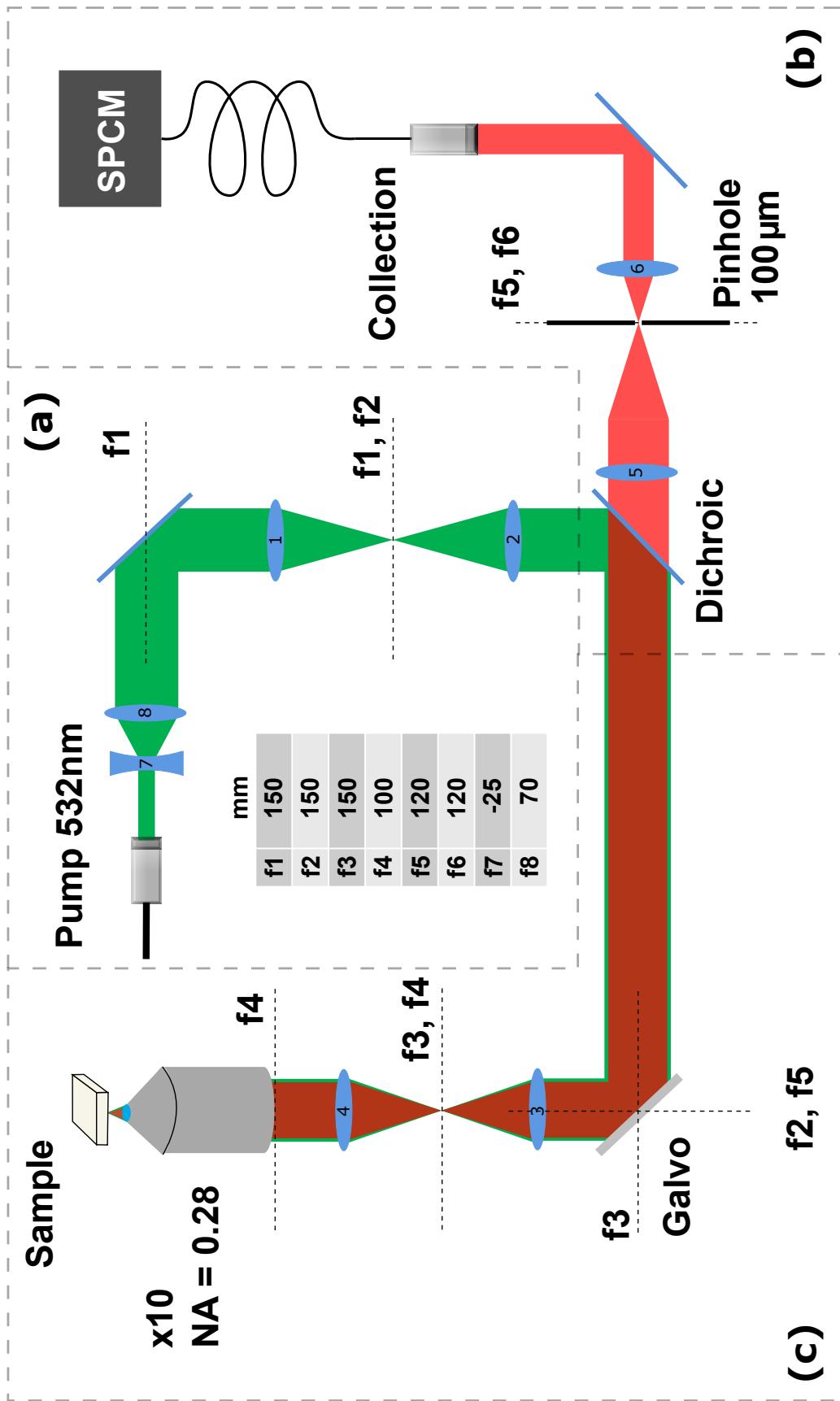


Figure 3-4: Confocal Microscope Custom built confocal microscope used to measure B_1 in LGR.

3.3.1 Experimental setup

To measure the field distribution within the LGR center loop a home-built scanning confocal microscope [Figure 3-5] was employed. The confocal microscope supplies the 532 nm pump beam to polarize the NVs and collects the resulting fluorescence using a dichroic beam splitter and a single photon counting module (SPCM). The three main sections of the experimental setup are the pump path, the collection path, and the sample path. The pump path [Figure 3-4 (a)] includes all optics from the launch of the excitation beam to the dichroic. Optical pulsing is accomplished using an acousto-optic modulator (AOM) that is located before the fiber launch; Ie. the laser passes through an AOM and is then coupled into a single mode (SM) polarization maintaining fiber which is then launched as the pump beam. The SM fiber picks off the first order refracted beam of the AOM and rejects the rest so no iris needed. The pump path contains a fiber launch (FiberPort coupler PAF-X-11-B), a half wave plate to selectively excite and address NV orientations, a beam expander consisting of a positive and negative focal length lens, and a 1:1 telescope. The 1:1 telescope (ie. no magnification) serves to change the angle of the beam down the sample path without moving the excitation spot off the galvo mirrors. In order for this to happen, the distance between the center of the two galvo mirrors and the last lens of the telescope must be equal to the focal length of the lens. In this way the angle of the beam into the objective can be changed without needing to reposition the galvos—which is a function designed for convenience only. The beam expander changes the collimation of 532 nm into the objective and therefore changes where the green comes into focus along the optical axis of the objective. This effectively serves to overlap the green excitation and the red fluorescence. Overlapping the two beams serves to maximize collection through the pinhole on the collection arm since the pinhole is initially aligned using the back-reflected green pump laser.

The collection path (or arm) [Figure 3-4 (b)] begins at the dichroic and ends at the collection end through a multimode fiber (65 μm core) and into the SPCM. The path consists of the dichroic, a pinhole between two telescoping lenses, a multimode fiber,

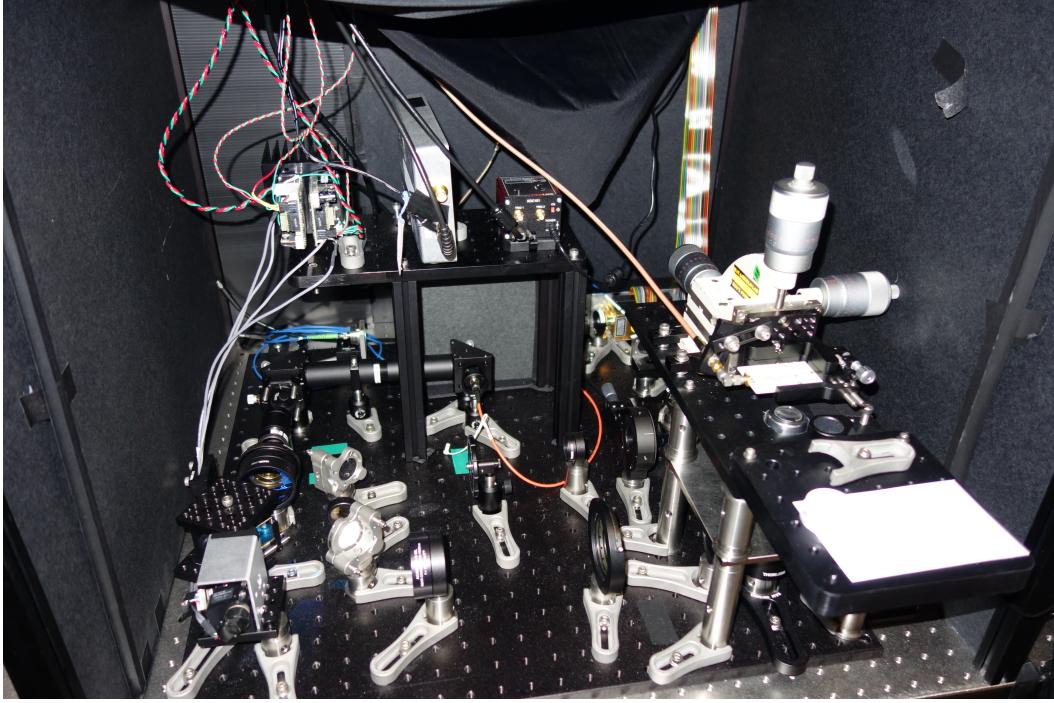


Figure 3-5: Image of Scanning Confocal Microscope Custom built scanning confocal microscope used to measure the B_1 distribution in the LGR

and an SPCM. The dichroic (Semrock Brightline FF552-Di02-25x36) filters the green pump beam from the sample fluorescence by reflecting wavelengths below 552nm and transmitting everything above. The first lens of the telescope focuses the beam down and passes it through a pinhole that spatially filters the image in X and Y to provide improved resolution. The pinhole was chosen to be 100 μm to maximize collection while sacrificing some lateral resolution in the image. Generally the pinhole diameter (p_d) should be selected using the following equation:

$$p_d = \frac{1.22\lambda}{NA} \cdot M_{objective} \cdot M_{telescope}. \quad (3.6)$$

The telescope in the sample path de-magnifies the beam by a factor $M_{telescope} = \frac{100}{150} = 0.67$ which is the ratio of the focal lengths of the lenses in the sample path. The objective used has a magnification of x10 which leads to a nominal pinhole size of 20 μm . However, this limits the amount of fluorescence collected because the pinhole filters out-of-focal-plane light which constitutes a large part of the signal. Since

measuring the B_1 field distribution in the LGR center cavity does not require high spatial resolution, a 100 μm diameter pinhole was chosen such that each measurement wasn't fluorescence starved. The filtered beam then passes through a second lens which focuses it onto the core of a multimode fiber connected to the SPCM. The multimode fiber allows for some rejection of ambient light without too much loss of the fluorescence signal. To further minimize the collection of ambient light, the multimode fiber dock and SPCM are enclosed in a light tight box.

The sample path [Figure 3-4 (c)] also begins at the dichroic, but passes through the galvanometer and objective and ends at the sample within the LGR center loop. It consists of a galvanometer, a 4F lens system (telescope), an iris, an objective and a sample stage. The objective used (Mitutoyo 378-803-3, M Plan Apo 10x NA = 0.28) has a long working distance of 34 mm. The long working distance was necessary to minimize perturbations of the B_1 field by the metal housing of the objective. Future NV wide-field imaging applications may require ceramic-tipped objectives. Finally, although this microscope has a galvanometer capable of scanning the beam over an area of $\sim 250 \mu\text{m} \times 250 \mu\text{m}$ the beam was held steady and the resonator moved to ensure B_0 is consistent for all measurements across the central loop of the LGR.

3.3.2 Measurement process

The strength and homogeneity of B_1 within the LGR central loop is evaluated employing standard NV techniques, as described in detail if references [57, 12, 47]. More specifically, a custom built scanning confocal microscope (as described in section 3.3.1) measures the Rabi nutation frequency Ω_R of an ensemble of NV centers. A {100}-cut diamond plate containing $\sim 1 \times 10^{14}$ NV/cm³ is mounted at the center of the LGR with the <100> crystallographic axis collinear with the LGR axis. A rare earth magnet creates a static magnetic bias field B_0 , which shifts the energies of the $m_s = \pm 1$ ground-state Zeeman sublevels. The energy shifts are given to first order by [72]

$$\Delta E \approx g_s \mu_B m_s \vec{B}_0 \cdot \hat{n}_i, \quad (3.7)$$

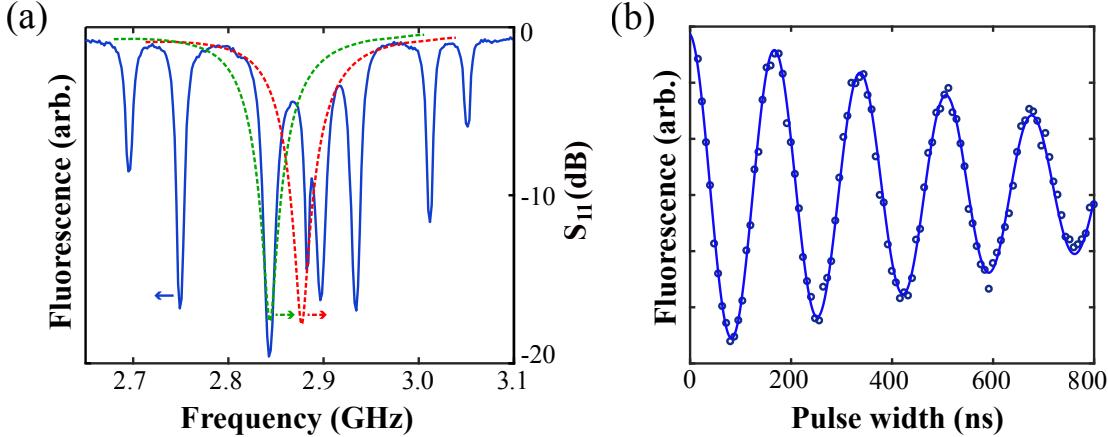


Figure 3-6: **LGR driving of an NV ensemble** **(a)** NV electron spin resonance spectrum (—) under application of bias field B_0 . The bias field allows individual addressing of all eight NV resonances, arising from the combination of the two allowed magnetic dipole transitions with the four possible NV orientations. The NV hyperfine structure is obscured by MW power broadening and the contrast variation between the NV resonances is attributed primarily to the S_{11} line-shape. The S_{11} parameter is shown before (---) and after (- - -) shifting the LGR resonant frequency f_0 to the target NV resonance. Arrows indicate corresponding y axes. **(b)** Typical data depicting Rabi oscillations under MW excitation at the target NV resonance frequency indicated in (a). Data (○) is fit (—) to an exponentially decaying sinusoid.

where \hat{n}_i denotes a unit vector oriented along one of the four diamond crystallographic axes. By judicious choice of \vec{B}_0 , all eight energy levels and associated $m_s=0 \leftrightarrow m_s = \pm 1$ magnetic dipole transitions can be isolated as shown in Fig. 3-6(a). The resonator is tuned to excite a single NV transition, yielding Rabi oscillations [Fig. 3-6(b)]. The data is fit to an exponentially decaying sinusoid in order to extract the Rabi frequency Ω_R , from which the magnitude of B_1 can be calculated as

$$B_1 = \sqrt{3} \frac{\hbar\Omega_R}{g_s \mu_B}. \quad (3.8)$$

In this geometry, the B_1 field is oriented along the [100] crystallographic axis of the diamond, degenerately offset from all four NV axis orientations by half the tetrahedral bond angle $\theta_{\text{tet}}/2 = \text{ArcCos}\frac{1}{\sqrt{3}} \approx 54^\circ$. NV Rabi oscillations are driven by the B_1 field component transverse to the NV symmetry axis, reducing the Rabi frequency by $\sqrt{2/3}$ [64]. Accounting for the rotating wave approximation introduces another

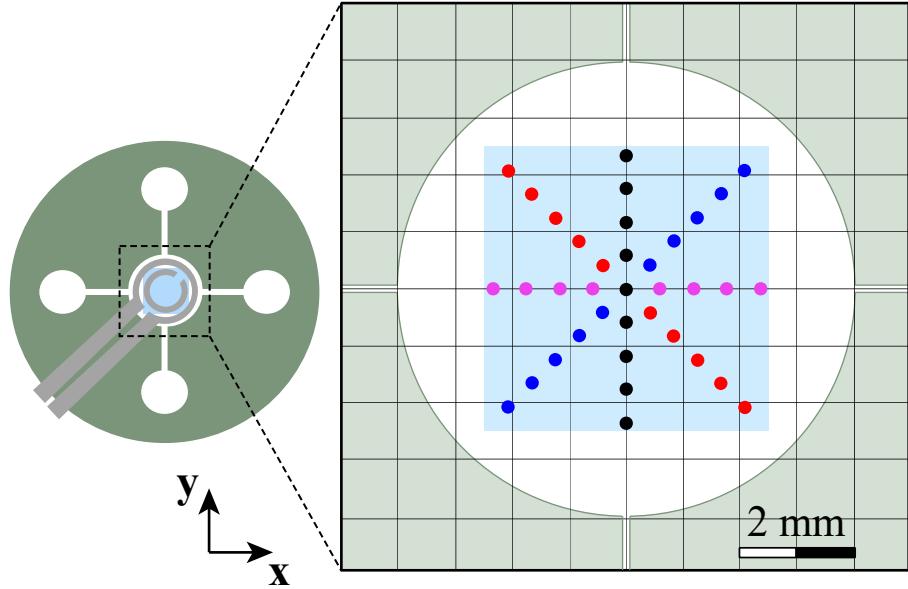


Figure 3-7: **Locus of Measurement Points** An NV-containing $4.5\text{ mm} \times 4.5\text{ mm}$ diamond plate is placed in the LGR central loop, and the Rabi frequency is measured where indicated ($\color{red}{\bullet}$, $\color{black}{\bullet}$, $\color{pink}{\bullet}$, $\color{blue}{\bullet}$) to characterize B_1 .

factor of $1/\sqrt{2}$ resulting in the conversion factor $\sqrt{3}$ in equation 3.8. To ensure \vec{B}_0 is consistent for all measurements across the LGR central loop, the confocal excitation volume is held fixed with respect to the B_0 -generating permanent magnet, and the diamond and LGR composite device are translated together. The process is then repeated at a locus of points within the LGR center loop (discussed below in section 3.4).

3.4 LGR field distribution

The measurement described above is applied at a locus of points in the center of the LGR [Figure 3-7]. Since the field distribution is radially symmetric the rest of the field values can be determined from the provided measurements. Application of incident MW power $P \approx 42\text{ dBm}$ yields an axially oriented B_1 at the center of the LGR with magnitude 4.7 G. The corresponding Rabi frequency $\Omega_R = 2\pi \times 7.7\text{ MHz}$ for NV centers oriented at half the tetrahedral bond angle relative to the LGR axis. Qualitatively, as shown in Figure 3-8 B_1 (calculated using equation 3.8) displays a minimum at

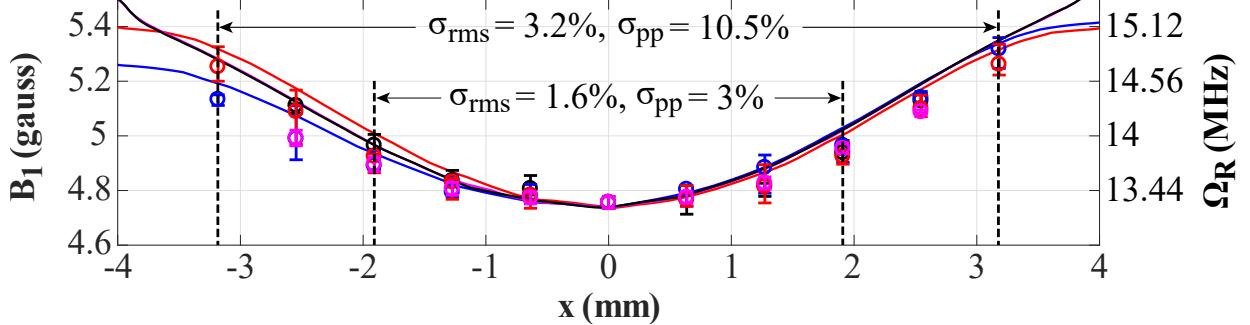


Figure 3-8: **B_1 field uniformity of LGR composite device.** B_1 field measurements (○,○,○,○) at the points depicted in 3-7 and simulations (—, —, —) along each locus of points are in good agreement. Error bars indicate 1-sigma uncertainty for the B_1 measurement. Dashed lines indicate the radial boundaries of the 32 mm² and 11 mm² areas over which B_1 field uniformity is evaluated. The measured B_1 uniformity is given for each area.

the LGR center, increases in magnitude with increasing radial displacement from the center, and is approximately radially symmetric. The best homogeneity is therefore expected at the LGR center. Using equations 3.4 and 3.5 we calculate that, over a 32 mm² circular area axially centered in the LGR central loop, we observe $\sigma_{rms} = 3.2\%$ and $\sigma_{pp} = 10.5\%$, as shown in Figure 3-8. Over a smaller 11 mm² circular area, a $\sigma_{rms} = 1.6\%$ and $\sigma_{pp} = 3\%$ is observed. Additionally, as a three-dimensional cavity resonator, the LGR provides better axial field uniformity than planar-only geometries [44, 40, 3]. For example, for a 3.14 mm³ cylindrical volume (1 mm radius disk with 1 mm thickness), simulations yield $\sigma_{rms} = 0.8\%$, $\sigma_{pp} = 3.7\%$ and an average B_1 of 4.8 G (see section 3.2).

Chapter 4

Discussion and Outlook

The device presented here exhibits further benefits which we now discuss, along with extensions tailored for specific applications. For example, for ubiquitously employed pulsed measurement protocols, a short ring-down time τ_{ring} (i.e., B_1 field $1/e$ decay time) is necessary for high-fidelity pulse shape control. Although techniques to compensate for long ring-down times are effective [71, 7, 54], shorter native values of τ_{ring} are nonetheless generally desired [56, 61]. The observed loaded quality factor $Q_L = 36$ corresponds to a ring-down time of $\tau_{\text{ring}} = 4$ ns (see section 3.1.1), making the device suitable for standard pulsed protocols [69, 38]. Additionally, a device manufactured with a smaller central loop featured in the appendix section A.1 achieves $Q_L = 25.4$ corresponding to a τ_{ring} of 2.8 ns.

Due to the square-root scaling of B_1 with an incident MW power ($B_1 \propto \sqrt{P}$), higher power handling can allow for stronger B_1 fields. The non-planar resonator design allows for otherwise higher incident MW powers as currents circulate over an extended 2D surface (versus the 1D edge for a planar structure). Furthermore, the metallic LGR thermal mass and thermal conductivity allow for efficient heat transfer and sinking, which results in improved device stability and power handling. Although the latter was not tested, the LGR composite device is expected to allow >100 W for CW and pulsed operation, limited by the dielectric breakdown of air in the 260 μm capacitive gaps. Should available MW power be constrained, stronger B_1 strengths can be achieved by fabricating the LGR from a more electrically conductive

material (e.g. silver or copper) at the expense of bandwidth (see section A.2). In such circumstances, the bandwidth can be continuously adjusted above its minimum value by over-coupling the resonator (at the expense of reduced Q_L).

While the presented LGR is 5 mm thick, the fundamental hole-and-slot approach is expected to be feasible for a variety of thicknesses. A thicker device will provide better field uniformity at the expense of optical access. In contrast, for applications requiring MW delivery over a thin planar volume, we expect the LGR can be fabricated via deposition on an appropriate insulating substrate, as discussed in Refs. [73, 74]. We have found semi-insulating silicon carbide [66] suitable due to the material's high thermal conductivity ($\approx 490 \text{ W}/(\text{m}^*\text{K})$) [32, 60], high Young's modulus, moderate cost and wide availability in semi-conductor grade wafers. Our simulations suggest the planar LGR approach can offer modest improvements in B_1 homogeneity over split-ring resonators.

Although the exciter antenna (see Section 2.3.3) facilitates a compact, vibration-resistant, and portable device, this component introduces non-idealities in both the field uniformity and optical access. As similar scattering parameters are obtained by inductively coupling a small coil to one of the LGR outer loops, this latter solution may find favor for applications requiring maximal optical access and, furthermore, requires no PCB fabrication.

In this work, we demonstrated a broadband tunable LGR allowing application of strong homogeneous MW fields to an NV ensemble. The LGR demonstrates a dramatic improvement over prior MW delivery mechanisms, both improving on and spatially extending MW field homogeneities. We expect the device to be useful for bulk sensing [1, 77, 15, 10, 5] and particularly imaging applications [41, 31, 5, 45, 79, 27, 30], due to the optical access allowed by the LGR composite device both above and below the diamond.

Appendix A

LGR variations

A.1 Smaller Cavity LGR

To achieve stronger MW driving, we also designed and fabricated smaller LGR with central loop radius $r_c = 2.5$ mm and $n = 4$ outer loops of radius $r_o = 2.45\text{mm}$, as shown in Figure A-1. The naked air-gapped LGR cavity exhibits $f_0 = 4.5$ GHz, similar to the larger LGR design described in the main text. Employing the same

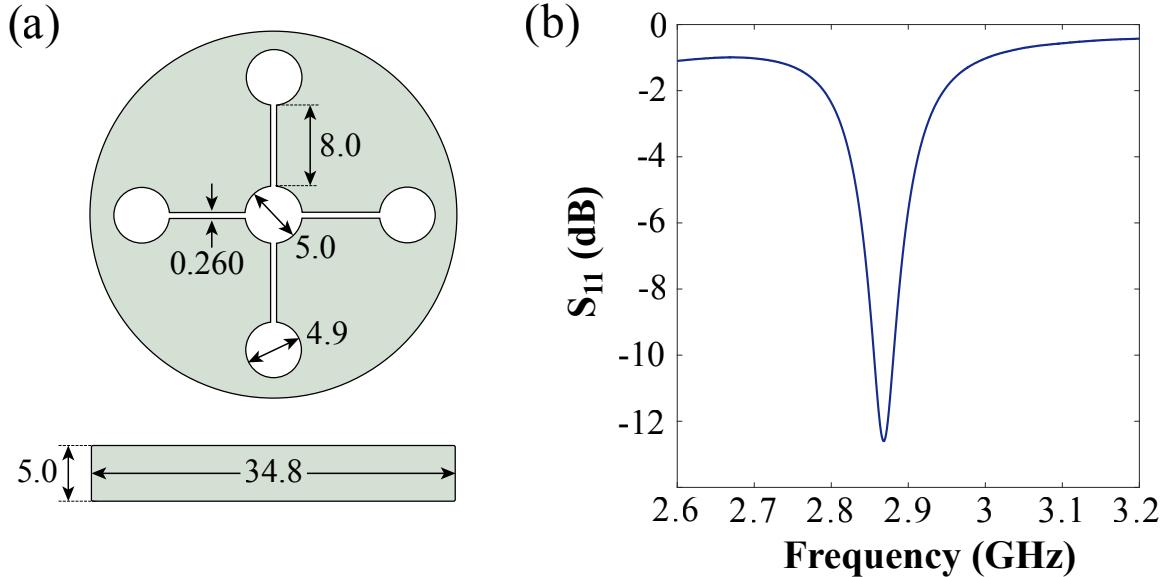


Figure A-1: **Smaller LGR design** (a) Line drawing of smaller LGR with central loop radius $r_c = 2.5$ mm as described in section A.1. Units are in mm. (b) Measured S_{11} for composite device tuned to $f_0 \approx 2.87\text{GHz}$.

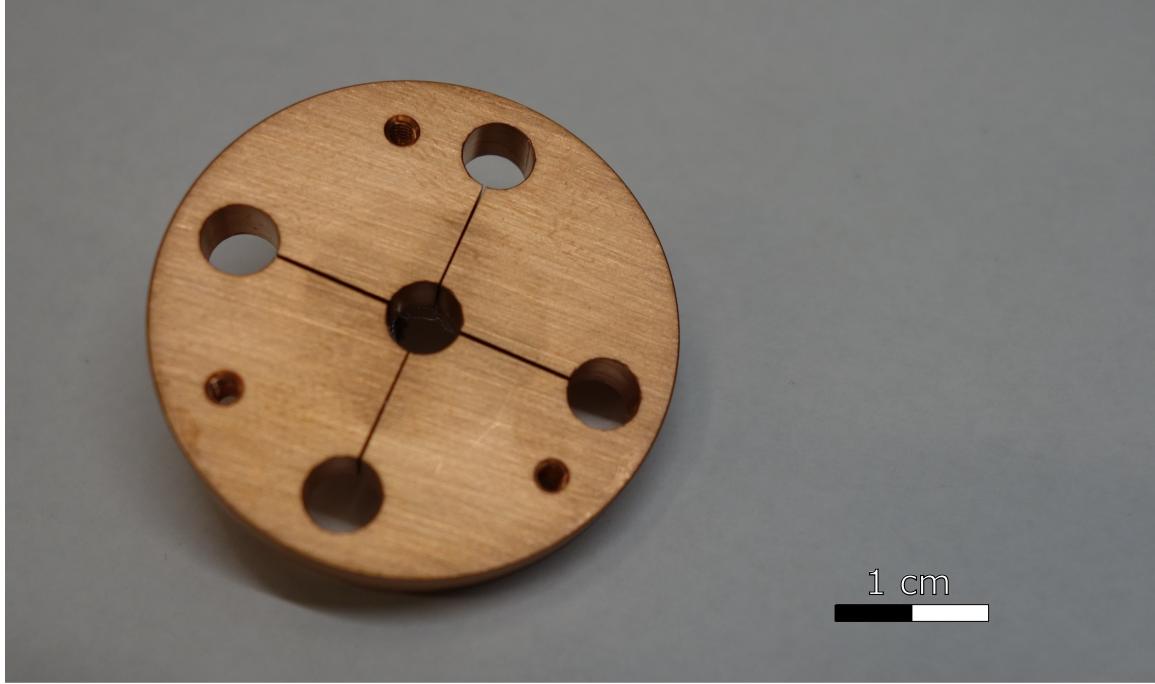


Figure A-2: **Copper Loop Gap Resonator** Loop Gap Resonator manufactured from C145 machinable copper

exciter antenna, we measure $B_1 = 5.8$ gauss at the center of the smaller LGR device; the measured 3dB bandwidth $\Delta_{3dB} = 112$ MHz corresponds to a loaded quality factor of $Q_L = 25.4$, and an associated ring-down time of 2.8 ns.

A.2 Copper LGR

To achieve higher Q-factors without redesigning the LGR geometry one can fabricate the device from a more conductive material such as copper ($\sigma_c = 59 \times 10^6$). We manufactured an LGR in C145 machinable copper [Figure A-2]. Figure A-3 plots the reflection coefficient S_{11} of both the copper and titanium LGR. Both are critically coupled and the Q factor (for the copper LGR) is measured to be 287, a $> \times 10$ improvement over the titanium device. Such an LGR can be desirable when bandwidth is not a limiting actor and stronger fields are required. The copper LGR has the same dimensions as the smaller cavity LGR in section A.1 that exhibits a Q of 25.4. Re-scaling the measured B_1 in the LGR center by $\sqrt{287}/\sqrt{25.4}$ yields the theoretical

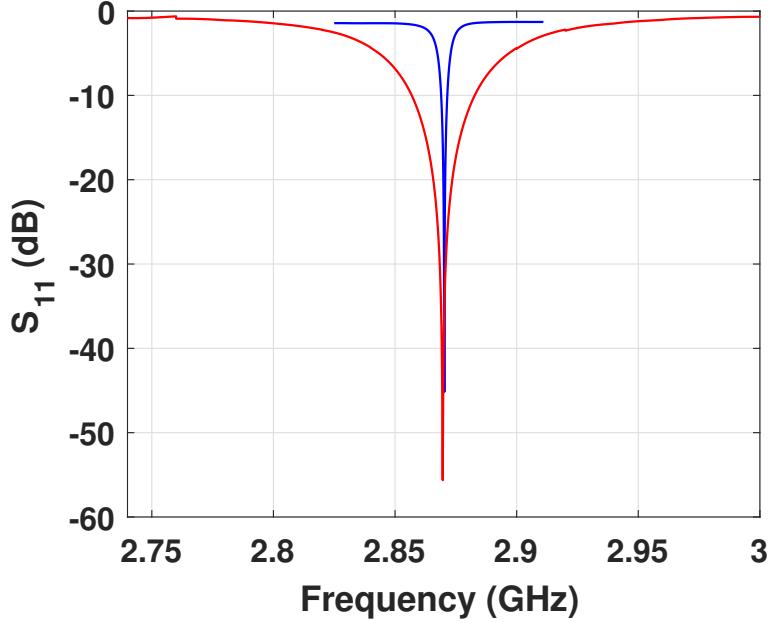


Figure A-3: **Copper vs. Titanium LGR** Scattering parameters (S_{11}) of the copper manufactured LGR (—) in comparison to titanium LGR (—)

field strength in the center of the copper resonator. In this case we predict the copper resonator to have a B_1 field strength of ~ 19.5 gauss in the center of the center loop.

A.3 Shielding

Fields that extended away from the LGR (ie. fields that aren't fully caught by the flux return loops) as well as fringing fields above and below the resonator can lead handshaking or radiation losses if the resonator is not properly shielded during operation. However, because shielding limits the optical accessibility of the center loop and because bandwidth optimization is not the primary concern for the LGR's use as a MW drive source for NVs, shielding was not addressed during the experiment outlined in section 3.3.2. For the sake of completeness however, it should be mentioned that proper lateral shielding of the LGR can increase Q factors by minimizing the aforementioned loss mechanisms [55, 61]. Using a copper tube approximately $\times 1.5$ the full diameter of the LGR, an almost doubling of the LGR Q factor (from 287 to ~ 470) was achieved.

Bibliography

- [1] V. M. Acosta, E. Bauch, M. P. Ledbetter, C. Santori, K.-M. C. Fu, P. E. Barclay, R. G. Beausoleil, H. Linget, J. F. Roch, F. Treussart, S. Chemerisov, W. Gawlik, and D. Budker. Diamonds with a high density of nitrogen-vacancy centers for magnetometry applications. *Physical Review B*, 80(11):115202, September 2009.
- [2] Paolo Andrich, F Charles, Xiaoying Liu, Hope L Bretscher, Jonson R Berman, F Joseph Heremans, Paul F Nealey, and David D Awschalom. [Long-range spin wave mediated control of defect qubits in nanodiamonds](#). *npj Quantum Information*, 3(1):28, 2017.
- [3] A. Angerer, T. Astner, D. Wirtitsch, H. Sumiya, S. Onoda, J. Isoya, S. Putz, and J. Majer. Collective strong coupling with homogeneous Rabi frequencies using a 3D lumped element microwave resonator. *Applied Physics Letters*, 109(3):033508, July 2016.
- [4] Gopalakrishnan Balasubramanian, IY Chan, Roman Kolesov, Mohannad Al-Hmoud, Julia Tisler, Chang Shin, Changdong Kim, Aleksander Wojcik, Philip R Hemmer, Anke Krueger, et al. [Nanoscale imaging magnetometry with diamond spins under ambient conditions](#). *Nature*, 455(7213):648, 2008.
- [5] J. F. Barry, M. J. Turner, J. M. Schloss, D. R. Glenn, Y. Song, M. D. Lukin, H. Park, and R. L. Walsworth. Optical magnetic detection of single-neuron action potentials using quantum defects in diamond. *Proceedings of the National Academy of Science*, 113:14133–14138, December 2016.
- [6] K. Bayat, J. Choy, M. Farrokh Baroughi, S. Meesala, and M. Loncar. Efficient, Uniform, and Large Area Microwave Magnetic Coupling to NV Centers in Diamond Using Double Split-Ring Resonators. *Nano Letters*, 14:1208–1213, March 2014.
- [7] T. W. Borneman and D. G. Cory. Bandwidth-limited control and ringdown suppression in high-Q resonators. *Journal of Magnetic Resonance*, 225:120–129, December 2012.
- [8] J. D. Breeze, J. Sathian, E. Salvadori, N. McN. Alford, and C. W. M. Kay. Continuous-wave room-temperature diamond maser. *ArXiv e-prints*, October 2017.

- [9] H. Y. Carr and E. M. Purcell. Effects of Diffusion on Free Precession in Nuclear Magnetic Resonance Experiments. *Physical Review*, 94:630–638, May 1954.
- [10] Georgios Chatzidrosos, Arne Wickenbrock, Lykourgos Bougas, Nathan Leefer, Teng Wu, Kasper Jensen, Yannick Dumeige, and Dmitry Budker. Miniature cavity-enhanced diamond magnetometer. *Phys. Rev. Applied*, 8:044019, Oct 2017.
- [11] Lilian Childress and Ronald Hanson. Diamond nv centers for quantum computing and quantum networks. *MRS bulletin*, 38(2):134–138, 2013.
- [12] Lilian Isabel Childress. *Coherent manipulation of single quantum systems in the solid state*. PhD thesis, March 2007.
- [13] M. Chipaux, A. Tallaire, J. Achard, S. Pezzagna, J. Meijer, V. Jacques, J.-F. Roch, and T. Debuisschert. Magnetic imaging with an ensemble of nitrogen vacancy-centers in diamond. *European Physical Journal D*, 69:166, July 2015.
- [14] H. Clevenson, L. M. Pham, C. Teale, K. Johnson, D. Englund, and D. Braje. Robust High-Dynamic-Range Vector Magnetometry via Nitrogen-Vacancy Centers in Diamond. *ArXiv e-prints*, February 2018.
- [15] H. Clevenson, M. E. Trusheim, C. Teale, T. Schröder, D. Braje, and D. Englund. Broadband magnetometry and temperature sensing with a light-trapping diamond waveguide. *Nature Physics*, 11:393–397, May 2015.
- [16] George Briggs Collins. *Microwave magnetrons*, volume 6. McGraw-Hill Book Company, 1948.
- [17] D. L. Creedon, J.-M. Le Floch, M. Goryachev, W. G. Farr, S. Castelletto, and M. E. Tobar. Strong coupling between P 1 diamond impurity centers and a three-dimensional lumped photonic microwave cavity. *Physical Review B*, 91(14):140408, April 2015.
- [18] C. L. Degen. Scanning magnetic field microscope with a diamond single-spin sensor. *Applied Physics Letters*, 92(24):243111, June 2008.
- [19] M. W. Doherty, F. Dolde, H. Fedder, F. Jelezko, J. Wrachtrup, N. B. Manson, and L. C. L. Hollenberg. Theory of the ground-state spin of the NV⁻ center in diamond. *Physical Review B*, 85(20):205203, May 2012.
- [20] M. W. Doherty, N. B. Manson, P. Delaney, F. Jelezko, J. Wrachtrup, and L. C. L. Hollenberg. The nitrogen-vacancy colour centre in diamond. *Physics Reports*, 528:1–45, July 2013.
- [21] M. W. Doherty, N. B. Manson, P. Delaney, F. Jelezko, J. Wrachtrup, and L. C. L. Hollenberg. The nitrogen-vacancy colour centre in diamond. *Physics Reports*, 528:1–45, July 2013.

- [22] F. Dolde, H. Fedder, M. W. Doherty, T. Nöbauer, F. Rempp, G. Balasubramanian, T. Wolf, F. Reinhard, L. C. L. Hollenberg, F. Jelezko, and J. Wrachtrup. Electric-field sensing using single diamond spins. *Nature Physics*, 7:459–463, June 2011.
- [23] A Dréau, M Lesik, L Rondin, P Spinicelli, O Arcizet, J-F Roch, and V Jacques. Avoiding power broadening in optically detected magnetic resonance of single nv defects for enhanced dc magnetic field sensitivity. *Physical Review B*, 84(19):195204, 2011.
- [24] M. V. G. Dutt, L. Childress, L. Jiang, E. Togan, J. Maze, F. Jelezko, A. S. Zibrov, P. R. Hemmer, and M. D. Lukin. Quantum Register Based on Individual Electronic and Nuclear Spin Qubits in Diamond. *Science*, 316, June 2007.
- [25] J. M. Franck, R. P. Barnes, T. J. Keller, T. Kaufmann, and S. Han. Active cancellation - A means to zero dead-time pulse EPR. *Journal of Magnetic Resonance*, 261:199–204, December 2015.
- [26] W. Froncisz and J. S. Hyde. The loop-gap resonator: a new microwave lumped circuit ESR sample structure. *Journal of Magnetic Resonance*, 47:515–521, 1982.
- [27] Roger R. Fu, Benjamin P. Weiss, Eduardo A. Lima, Richard J. Harrison, Xue-Ning Bai, Steven J. Desch, Denton S. Ebel, Clément Suavet, Huapei Wang, David Glenn, David Le Sage, Takeshi Kasama, Ronald L. Walsworth, and Aaron T. Kuan. Solar nebula magnetic fields recorded in the semarkona meteorite. *Science*, 346(6213):1089–1092, 2014.
- [28] T. Gaebel, M. Domhan, I. Popa, C. Wittmann, P. Neumann, F. Jelezko, J. R. Rabeau, N. Stavrias, A. D. Greentree, S. Prawer, J. Meijer, J. Twamley, P. R. Hemmer, and J. Wrachtrup. Room-temperature coherent coupling of single spins in diamond. *Nature Physics*, 2:408–413, June 2006.
- [29] F. E. Gardiol. Open-ended waveguides - Principles and applications. *Advances in Electronics and Electron Physics*, 63:139–187, 1985.
- [30] David R Glenn, Roger R Fu, Pauli Kehayias, David Le Sage, Eduardo A Lima, Benjamin P Weiss, and Ronald L Walsworth. Micrometer-scale magnetic imaging of geological samples using a quantum diamond microscope. *Geochemistry, Geophysics, Geosystems*, 2017.
- [31] David R Glenn, Kyungheon Lee, Hongkun Park, Ralph Weissleder, Amir Yacoby, Mikhail D Lukin, Hakho Lee, Ronald L Walsworth, and Colin B Connolly. **Single-cell magnetic imaging using a quantum diamond microscope**. *Nature methods*, 12(8):736, 2015.
- [32] N. Haider Protik, A. Katre, L. Lindsay, J. Carrete, N. Mingo, and D. Broido. Phonon thermal transport in 2H, 4H and 6H silicon carbide from first principles. *ArXiv e-prints*, May 2017.

- [33] J. G. Hartnett, M. E. Tobar, E. N. Ivanov, and J. Krupka. Room temperature measurement of the anisotropic loss tangent of sapphire using the whispering gallery mode technique. *IEEE Transactions on Ultrasonics, Ferroelectrics, and Frequency Control*, 53(1):34–38, Jan 2006.
- [34] J. S. Hodges, N. Y. Yao, D. Maclaurin, C. Rastogi, M. D. Lukin, and D. Englund. Timekeeping with electron spin states in diamond. *Physical Review A*, 87(3):032118, March 2013.
- [35] V. R. Horowitz, B. J. Alemán, D. J. Christle, A. N. Cleland, and D. D. Awschalom. Electron spin resonance of nitrogen-vacancy centers in optically trapped nanodiamonds. *Proceedings of the National Academy of Science*, 109:13493–13497, August 2012.
- [36] A. Horsley, P. Appel, J. Wolters, J. Achard, A. Tallaire, P. Maletinsky, and P. Treutlein. Microwave device characterisation using a widefield diamond microscope. *ArXiv e-prints*, February 2018.
- [37] A. Ibarra, M. González, R. Vila, and J. Mollá. Wide frequency dielectric properties of CVD diamond. *Diamond and Related Materials*, 6:856–859, April 1997.
- [38] F. Jelezko, T. Gaebel, I. Popa, A. Gruber, and J. Wrachtrup. Observation of Coherent Oscillations in a Single Electron Spin. *Physical Review Letters*, 92(7):076401, February 2004.
- [39] Kasper Jensen, Pauli Kehayias, and Dmitry Budker. Magnetometry with Nitrogen-Vacancy Centers in Diamond. In *High Sensitivity Magnetometers*, pages 553–576. Springer, 2017.
- [40] P. Kapitanova, V. Soshenko, V. Vorobyov, D. Dobrykh, S. Bolshedvorskiih, V. Sorokin, and A. Akimov. Dielectric resonator antenna for coupling to NV centers in diamond. In *American Institute of Physics Conference Series*, volume 1874 of *American Institute of Physics Conference Series*, page 030017, September 2017.
- [41] S. Karaveli, O. Gaathon, A. Wolcott, R. Sakakibara, O. A. Shemesh, D. S. Peterka, E. S. Boyden, J. S. Owen, R. Yuste, and D. Englund. Modulation of nitrogen vacancy charge state and fluorescence in nanodiamonds using electrochemical potential. *Proceedings of the National Academy of Science*, 113:3938–3943, April 2016.
- [42] S. Kitazawa, Y. Matsuzaki, S. Saijo, K. Kakuyanagi, S. Saito, and J. Ishi-Hayase. Vector-magnetic-field sensing via multifrequency control of nitrogen-vacancy centers in diamond. *Physical Review A*, 96(4):042115, October 2017.
- [43] M. F. Koskinen and K. R. Metz. The concentric loop-gap resonator—A compact, broadly tunable design for NMR applications. *Journal of Magnetic Resonance*, 98:576–588, 1992.

- [44] J.-M. Le Floch, N. Delhote, M. Aubourg, V. Madrangeas, D. Cros, S. Castelletto, and M. E. Tobar. Towards achieving strong coupling in three-dimensional-cavity with solid state spin resonance. *Journal of Applied Physics*, 119(15):153901, April 2016.
- [45] D Le Sage, K Arai, DR Glenn, SJ DeVience, LM Pham, L Rahn-Lee, MD Lukin, A Yacoby, A Komeili, and RL Walsworth. [Optical magnetic imaging of living cells](#). *Nature*, 496(7446):486, 2013.
- [46] J. R. Maze, A. Gali, E. Togan, Y. Chu, A. Trifonov, E. Kaxiras, and M. D. Lukin. Properties of nitrogen-vacancy centers in diamond: the group theoretic approach. *New Journal of Physics*, 13(2):025025, February 2011.
- [47] J. Maze Rios. *Quantum manipulation of nitrogen-vacancy centers in diamond: From basic properties to applications*. PhD thesis, Harvard University, 2010.
- [48] M. Mehdizadeh and T. K. Ishii. Electromagnetic field analysis and calculation of the resonance characteristics of the loop-gap resonator. *IEEE Transactions on Microwave Theory Techniques*, 37:1113–1118, July 1989.
- [49] M. Mehdizadeh, T. K. Ishii, J. S. Hyde, and W. Froncisz. Loop-Gap Resonator: A Lumped Mode Microwave Resonant Structure. *IEEE Transactions on Microwave Theory Techniques*, 31:1059–1064, December 1983.
- [50] Mehrdad Mehdizadeh. An investigation on electromagnetic fields and properties of the loop-gap resonator, a lumped mode microwave resonant structure. 1983.
- [51] S. Meiboom and D. Gill. Modified Spin-Echo Method for Measuring Nuclear Relaxation Times. *Review of Scientific Instruments*, 29:688–691, August 1958.
- [52] M. Mrózek, J. Mlynarczyk, D. S. Rudnicki, and W. Gawlik. Circularly polarized microwaves for magnetic resonance study in the GHz range: Application to nitrogen-vacancy in diamonds. *Applied Physics Letters*, 107(1):013505, July 2015.
- [53] P. Neumann, I. Jakobi, F. Dolde, C. Burk, R. Reuter, G. Waldherr, J. Honert, T. Wolf, A. Brunner, J. H. Shim, D. Suter, H. Sumiya, J. Isoya, and J. Wrachtrup. High-Precision Nanoscale Temperature Sensing Using Single Defects in Diamond. *Nano Letters*, 13:2738–2742, June 2013.
- [54] A. S. Peshkovsky, J. Forguez, L. Cerioni, and D. J. Pusiol. RF probe recovery time reduction with a novel active ringing suppression circuit. *Journal of Magnetic Resonance*, 177:67–73, November 2005.
- [55] Sergey Petryakov, Michael Chzhan, Alexandre Samoilov, Guanglong He, Periannan Kuppusamy, and Jay L Zweier. A bridged loop-gap s-band surface resonator for topical epr spectroscopy. *Journal of Magnetic Resonance*, 151(1):124–128, 2001.

- [56] S. Pfenninger, W. Froncisz, J. Forrer, J. Luglio, and J. S. Hyde. General method for adjusting the quality factor of EPR resonators. *Review of Scientific Instruments*, 66:4857–4865, October 1995.
- [57] L. M. Pham. *Magnetic field sensing with nitrogen-vacancy color centers in diamond*. PhD thesis, Harvard University, 2013.
- [58] Linh My Pham, David Le Sage, Paul L Stanwix, Tsun Kwan Yeung, D Glenn, Alexei Trifonov, Paola Cappellaro, PR Hemmer, Mikhail D Lukin, Hongkun Park, et al. Magnetic field imaging with nitrogen-vacancy ensembles. *New Journal of Physics*, 13(4):045021, 2011.
- [59] W. Piasecki and W. Froncisz. Field distributions in loop-gap resonators. *Measurement Science and Technology*, 4:1363–1369, December 1993.
- [60] X. Qian, P. Jiang, and R. Yang. Anisotropic Thermal Conductivity of 4H and 6H Silicon Carbide Measured Using Time-Domain Thermoreflectance. *ArXiv e-prints*, December 2017.
- [61] George A. Rinard and Gareth R. Eaton. *Loop-Gap Resonators*. Kluwer Academic/Plenum Publishers, 2005.
- [62] L. Rondin, J.-P. Tetienne, T. Hingant, J.-F. Roch, P. Maletinsky, and V. Jacques. Magnetometry with nitrogen-vacancy defects in diamond. *Reports on Progress in Physics*, 77(5):056503, May 2014.
- [63] B. C. Rose, A. M. Tyryshkin, H. Riemann, N. V. Abrosimov, P. Becker, H.-J. Pohl, M. L. W. Thewalt, K. M. Itoh, and S. A. Lyon. Coherent Rabi Dynamics of a Superradiant Spin Ensemble in a Microwave Cavity. *Physical Review X*, 7(3):031002, July 2017.
- [64] Kento Sasaki, Yasuaki Monnai, Soya Saijo, Ryushiro Fujita, Hideyuki Watanabe, Junko Ishi-Hayase, Kohei M Itoh, and Eisuke Abe. [Broadband, large-area microwave antenna for optically detected magnetic resonance of nitrogen-vacancy centers in diamond](#). *Review of Scientific Instruments*, 87(5):053904, 2016.
- [65] R. Schirhagl, K. Chang, M. Loretz, and C. L. Degen. Nitrogen-Vacancy Centers in Diamond: Nanoscale Sensors for Physics and Biology. *Annual Review of Physical Chemistry*, 65:83–105, April 2014.
- [66] J. M. Schloss, J. F. Barry, M. J. Turner, and R. L. Walsworth. Simultaneous Broadband Vector Magnetometry Using Solid-State Spins. *ArXiv e-prints*, March 2018.
- [67] David A. Simpson, Robert G. Ryan, Liam T. Hall, Evgeniy Panchenko, Simon C. Drew, Steven Petrou, Paul S. Donnelly, Paul Mulvaney, and Lloyd C. L. Hollenberg. Electron paramagnetic resonance microscopy using spins in diamond under ambient conditions. *Nature Communications*, 8(1):458, 2017.

- [68] B. Smeltzer, J. McIntyre, and L. Childress. Robust control of individual nuclear spins in diamond. *Physical Review A*, 80(5):050302, November 2009.
- [69] B. Smeltzer, J. McIntyre, and L. Childress. Robust control of individual nuclear spins in diamond. *Physical Review A*, 80(5):050302, November 2009.
- [70] M. Steiner, P. Neumann, J. Beck, F. Jelezko, and J. Wrachtrup. Universal enhancement of the optical readout fidelity of single electron spins at nitrogen-vacancy centers in diamond. *Physical Review B*, 81(3):035205, January 2010.
- [71] Y. Tabuchi, M. Negoro, K. Takeda, and M. Kitagawa. Total compensation of pulse transients inside a resonator. *Journal of Magnetic Resonance*, 204:327–332, June 2010.
- [72] J. M. Taylor, P. Cappellaro, L. Childress, L. Jiang, D. Budker, P. R. Hemmer, A. Yacoby, R. Walsworth, and M. D. Lukin. High-sensitivity diamond magnetometer with nanoscale resolution. *Nature Physics*, 4:810–816, October 2008.
- [73] Y. Twig, E. Dikarov, and A. Blank. Ultra miniature resonators for electron spin resonance: Sensitivity analysis, design and construction methods, and potential applications. *Molecular Physics*, 111:2674–2682, October 2013.
- [74] Y. Twig, E. Suhovoy, and A. Blank. Sensitive surface loop-gap microresonators for electron spin resonance. *Review of Scientific Instruments*, 81(10):104703–104703–11, October 2010.
- [75] A. Sils W. B. Westphal. *Dielectric Constant and Loss Data*. Air Force Materials Laboratory, Air Force Systems Command, 4 1972.
- [76] Z.-H. Wang, G. de Lange, D. Ristè, R. Hanson, and V. V. Dobrovitski. Comparison of dynamical decoupling protocols for a nitrogen-vacancy center in diamond. *Physical Review B*, 85(15):155204, April 2012.
- [77] T. Wolf, P. Neumann, K. Nakamura, H. Sumiya, T. Ohshima, J. Isoya, and J. Wrachtrup. Subpicotesla Diamond Magnetometry. *Physical Review X*, 5(4):041001, October 2015.
- [78] R. L. Wood, W. Froncisz, and J. S. Hyde. The loop-gap resonator. II. Controlled return flux three-loop, two-gap microwave resonators for ENDOR and ESR spectroscopy. *Journal of Magnetic Resonance*, 58:243–253, 1984.
- [79] Yuzhou Wu, Fedor Jelezko, Martin B Plenio, and Tanja Weil. **Diamond quantum devices in biology**. *Angewandte Chemie International Edition*, 55(23):6586–6598, 2016.
- [80] L.-L. Yang, Q.-Q. Liu, X.-Y. Pan, and D.-M. Chen. Design and Application of a Near Field Microwave Antenna for the Spin Control of Nitrogen-Vacancy Centers. *Chinese Physics Letters*, 27(3):038401, March 2010.

- [81] Chen Zhang, Heng Yuan, Ning Zhang, Lixia Xu, Jixing Zhang, Bo Li, and Jiancheng Fang. Vector magnetometer based on synchronous manipulation of nitrogen-vacancy centers in all crystal directions. *Journal of Physics D: Applied Physics*, 51(15):155102, 2018.
- [82] Ning Zhang, Chen Zhang, Lixia Xu, Ming Ding, Wei Quan, Zheng Tang, and Heng Yuan. [Microwave magnetic field coupling with nitrogen-vacancy center ensembles in diamond with high homogeneity](#). *Applied Magnetic Resonance*, 47(6):589–599, 2016.